

# Coarse-scale constrained ensemble Kalman filter for subsurface characterization

S. Akella <sup>\*,a</sup> , A. Datta-Gupta <sup>b</sup> , Y. Efendiev <sup>c</sup>

<sup>a</sup>*Dept. of Earth & Planetary Sciences and Dept. of Applied Mathematics & Statistics, The Johns Hopkins University, Baltimore, MD 21218, USA*

<sup>b</sup>*Department of Petroleum Engineering, Texas A&M University, College Station, TX 77843, USA*

<sup>c</sup>*Department of Mathematics, Texas A&M University, College Station, TX 77843, USA*

---

## Abstract

In this paper we propose a way to integrate data at different spatial scales using the ensemble Kalman filter (EnKF), such that the finest scale data is sequentially estimated, subject to the available data at the coarse scale(s), as an additional constraint. Relationship between various scales has been modeled via upscaling techniques. The proposed coarse-scale EnKF algorithm is recursive and easily implementable. Our numerical results with static as well as dynamic, coarse-scale data provide improved fine-scale field estimates when compared to the results with regular EnKF (which did not incorporate the coarse-scale data). We also tested our algorithm with various precisions of the coarse-scale data to account for the inexact relationship between the fine and coarse scale data. As expected, the results show that higher precision in the coarse-scale data, yielded improved estimates.

### *Key words:*

Ensemble Kalman filter, Multiscale data, Upscaling models, Sequential data assimilation

---

\* Corresponding author. Address: Dept. of Earth & Planetary Sciences and Dept. of Applied Mathematics & Statistics, The Johns Hopkins University, Baltimore, MD 21218, USA

*Email address:* santha.akella@jhu.edu (S. Akella)

## 1 Introduction

The principal objective of data assimilation methods [28] is to combine the information provided by measured data and a (numerical) forecast model to obtain an improved estimate of the system state (and parameters). Unlike variational methods which require availability of complex adjoint models for data assimilation, the ensemble Kalman filter (**EnKF**) can be quickly implemented and one can also obtain uncertainty estimates via error variance-covariance propagation; see [21] and references therein for further details. The **EnKF** is a sequential Monte Carlo method based on Bayes theorem. The method is increasingly being used for estimating unknown model state and parameters in various geological and hydrological models [31,5,29].

Broadly speaking, the measured data used for description of reservoir porosity and permeability characterization consist of static and dynamic data. Static data such as well logs, core samples can resolve heterogeneity at a scale of a few inches or feet with high reliability. However, dynamic data such as fractional flow (defined as the ratio of the injection fluid to the total fluid produced at the production wells; or water cut), pressure transient and tracer test data typically scan the length scales comparable to the inter-well distances. Additional dynamic data such as time-lapse seismic images [30] can provide improved spatial sampling, but at a lower precision. A majority of previous studies on uncertainty quantification in reservoir performance forecasting using **EnKF** have mostly dealt with integration of dynamic data (for e.g., [32,35,24]). However it is widely recognized that integration of additional multiscale data could further reduce the uncertainty (see [27,14,15] and references therein). We also note that when compared to fine-scale simulations, coarse-scale simulations are many folds computationally efficient (for e.g., see introduction in [36]). With that perspective, integration of data at coarse-and fine-scales, is an important objective. We would like to emphasize that to the best of our knowledge, integration of multiscale data using **EnKF** to estimate fine-scale fields for subsurface characterization has not yet been addressed. Also, our method could be generalized to other sequential data assimilation methods such as particle filtering (where, rather than updating the ensemble members model state, we update the probability assigned to each ensemble member based on model data misfit). The main reason why we used **EnKF** in this paper is because it requires fewer ensemble members than the particle filters, see [29] and references therein for further details.

In this paper, apart from the water cut data, we consider two kinds of coarse-scale measured data as well. The coarse-scale data are assumed to be permeability and/or saturation at some specified level of precision. The unknown variables: permeability, at the fine-scale, are estimated using a modification to the **EnKF** algorithm, linking the data at different scales via upscaling. It

is important to resolve fine-scale heterogeneity for various purposes such as, enhanced oil recovery, environmental remediation, etc. The main idea behind upscaling is to obtain an *effective* coarse-scale permeability which yields the same average response as that of the underlying fine-scale field, locally. Single phase flow upscaling procedures for two phase flow problem have been discussed by many authors; see e.g., [6,3,11] and also Section 3.1. We will refer to our proposed variant of **EnKF** as *coarse-scale EnKF*. Assimilation using dynamic data, such as fractional flow data only, is therefore referred to as *regular EnKF*. First we consider coarse-scale permeability data, which can be obtained either from geologic consideration or coarse-scale inversion of dynamic, fractional flow data on a coarse grid as considered in [27,15]. We note that coarse-scale inversion of the dynamic data usually uses more accurate and reliable prior models and, thus, the inversion results have higher precision. In Section 5 we illustrate a procedure for such a coarse-scale inversion. This coarse-scale, static data can be viewed as a *constraint*, which is to be satisfied up to the prescribed variance for obtaining the fine-scale estimates in every data assimilation cycle. Upscaling methods relate the solution at the fine-scale to the coarse-scale, therefore in the Kalman filter context, it amounts to modeling a nonlinear observation operator. In our coarse-scale **EnKF** approach, we use the measured data in batches, such that the estimate with one data becomes a prior while assimilating the other observation (see Section 3 for further details). Though in this paper we used coarse-scale data at only one scale, our approach can be easily generalized to assimilate data at multiple scales by appropriately modeling the linkage between different scales.

The second kind of coarse-scale observed data we consider is dynamic, and is motivated based on the increasing availability of time-lapse seismic images (or 4d seismic data). Integration of inverted 4d seismic data (at fine-scale) using the **EnKF** has been addressed in [9] and [34]. In this article, we consider the seismic data, not to correspond to the finest scale, but to a coarse-scale, since time-lapse seismic data typically will have a lower resolution compared to the fine-scale geologic model [22]. As the time-lapse seismic data is collected only at specific time intervals, we used coarse-scale fluid saturation, as measured data to be available at a prescribed level of precision (which accounts for the inaccuracies involved in inversion of 4d seismic data) and only for certain assimilation cycles. Therefore unlike the coarse-scale static permeability data considered earlier, the coarse-scale saturation data is assimilated only in certain assimilation cycles (see Section 4.3 for details).

For the purpose of self-contendness and notational clarity, we briefly review the governing equations, sequential data assimilation using the ensemble Kalman filter in Section 2, which is followed by a description of the coarse-scale **EnKF** algorithm (Section 3). For our numerical results (Section 4), we consider a five-spot pattern, with the injection well placed in the middle of a rectangular domain and four production wells located at the vertices of the rectangle.

A reference case is used to provide *true* data, which is randomly perturbed to obtain synthetic measurements. A comparison of the regular EnKF with the coarse-scale EnKF (Sections 4.1 and 4.2 respectively) shows that using coarse-scale permeability data (via coarse-scale EnKF) significantly improves the fine-scale estimates as well as future fractional flow prediction. We obtained similar improvements with coarse-scale saturation data (Section 4.3). But due to the fact that it was assimilated infrequently, the fine-scale estimates and prediction is not as good as using coarse-scale permeability, nevertheless better than those obtained using regular EnKF. In Section 5, we demonstrate that the coarse-scale permeability data can be obtained in the absence of any prior geologically derived or coarse-scale inverted permeability data. To accomplish this, we first develop a model which maps fine-scale to coarse-scale water cuts. Thereafter, the mapped coarse-scale water cut is used to estimate the coarse-scale permeability field.

## 2 Preliminaries

### 2.1 Fine-scale model

In this paper, we consider two-phase flow in a subsurface formation under the assumption that the displacement is dominated by viscous effects. For simplicity, we neglect the effects of gravity, compressibility, and capillary pressure, although our proposed approach is independent of the choice of physical mechanisms. Also, porosity will be considered to be constant. The two phases will be referred to as water and oil (or a non-aqueous phase liquid), designated by subscripts  $w$  and  $o$ , respectively. We write Darcy's law for each phase as follows:

$$\mathbf{v}_j = -\frac{k_{rj}(S)}{\mu_j} \boldsymbol{\kappa}_f \nabla pr, \quad (1)$$

$$\nabla \cdot (\lambda(S) \boldsymbol{\kappa}_f \nabla pr) = h, \quad (2)$$

$$\lambda(S) = \frac{k_{rw}(S)}{\mu_w} + \frac{k_{ro}(S)}{\mu_o}, f(S) = \frac{k_{rw}(S)/\mu_w}{k_{rw}(S)/\mu_w + k_{ro}(S)/\mu_o},$$

$$\mathbf{v} = \mathbf{v}_w + \mathbf{v}_o = -\lambda(S) \boldsymbol{\kappa}_f \cdot \nabla pr, \quad (3a)$$

$$\phi \frac{\partial S}{\partial t} + \mathbf{v} \cdot \nabla S = 0. \quad (3b)$$

The above descriptions are referred to as the fine-scale model of the two-phase flow problem. Here  $\boldsymbol{\kappa}_f$  is the (fine-scale) permeability of the medium,  $\lambda(S)$  is the total mobility,  $\mu_j$  denotes phase viscosity,  $pr$  is the pressure,  $h$  is the source term,  $\phi$  and  $S$  denote porosity and water saturation (volume fraction), respectively.

## 2.2 Sequential estimation using **EnKF**

Using dynamic measured data such as water cut, we can sequentially estimate the unknown parameters (permeability, porosity, etc.) and state variables such as pressure, water saturation (two-phase flow) and production data at well locations using the **EnKF** as discussed in [32,23,24,8,2,21]. Following these previous works, in this paper we assume that the only dynamic data available is water cut data, and that porosity is known. The combined state-parameter to be estimated are given by  $\Psi = [\ln(\kappa_f), \mathbf{pr}, \mathbf{S}, \mathbf{W}_c]^T$ . Where  $\ln(\cdot)$  is natural logarithm of permeability field and  $\mathbf{W}_c$  denotes water cut; in order to distinguish observed water cut from model predicted water cut, now onwards we will denote the observed water cut data  $\mathbf{W}_c^o$ , by  $\mathbf{y}$ .

The **EnKF** introduced by Evensen, 1994 [20] is a sequential Monte Carlo method where an ensemble of model states evolve in state-space with mean as the best estimate and spread of the ensemble as the error covariance, as summarized in the following steps. Each of the ensemble members is forecasted independently (in this work, we neglected modeling errors),

$$\Psi_{n+1}^{(i)} = F[\Psi_n^{(i)}], \quad (4)$$

where  $F[\cdot]$  is the forecast operator (eqns. 1–3b), superscript  $(i)$  denotes the  $i^{th}$  ensemble member; now onwards we will drop the time subscript. The ensemble mean and covariance are defined as,

$$\bar{\Psi} = \frac{1}{N_e} \sum_{i=1}^{N_e} \Psi^{(i)}, \quad (5a)$$

$$\mathbf{P}^f \approx \frac{1}{N_e - 1} \mathbf{A}' (\mathbf{A}')^T, \quad (5b)$$

where  $\mathbf{A}' = (\mathbf{b}^{(1)}, \mathbf{b}^{(2)}, \dots, \mathbf{b}^{(N_e)})$ ,  $\mathbf{b}^{(i)} = \Psi^{(i)} - \bar{\Psi}$ , and  $N_e$  is the number of ensemble members. The observation vector for each ensemble member is given by,

$$\mathbf{y}^{(i)} = \mathbf{H}[\Psi^t] + \nu^{(i)}, \quad (6)$$

where  $\mathbf{H}[\Psi^t]$  is the observed data from the truth and  $\nu^{(i)}$  represents observational errors, which are *i.i.d.* samples [4] from a normal distribution with zero mean and variance,  $\mathbf{R}$ . We note that if only the water cut data is being measured, the mapping from model-to-observational space,  $\mathbf{H}$  is trivially equal to  $[\mathbf{0} \ \mathbf{0} \ \mathbf{0} \ \mathbf{I}]$ , since  $\Psi = [\ln(\kappa), \mathbf{pr}, \mathbf{S}, \mathbf{W}_c]^T$ .

The forecasted ensemble (eqn. 4) is updated by assimilating the observed data,

$$\widetilde{\Psi}^{(i)} = \Psi^{(i)} + \mathbf{K}(\mathbf{y}^{(i)} - \mathbf{H}[\Psi^{(i)}]), \quad (7)$$

where  $\mathbf{K}$  is the Kalman gain, given by

$$\mathbf{K} = \mathbf{P}^f \mathbf{H}^T [\mathbf{H} \mathbf{P}^f \mathbf{H}^T + \mathbf{R}]^{-1}.$$

Computationally efficient implementation of the EnKF is discussed for e.g., in [21,5]. We use the above set of corrected ensemble states,  $\{\widetilde{\Psi}^{(i)}\}_{i=1}^{N_e}$  in the simulation model (eqn. 4) to predict until the next set of observational data is available.

### 3 Coarse-scale constrained EnKF

The EnKF presented so far, used only the dynamic, production data (water cut)  $\mathbf{y}$ , with error  $\boldsymbol{\nu} = \mathbf{y} - \mathbf{H}[\Psi^t]$ ,  $\boldsymbol{\nu} \sim \mathcal{N}(\mathbf{0}, \mathbf{R})$  to update the ensemble (eqn. 7). In addition to  $\mathbf{y}$ , if we are also given static data (as mentioned in the Introduction), which is another set of independently measured data,  $\mathbf{z}$ . Assuming that the corresponding measurement error is given by  $\boldsymbol{\omega} = \mathbf{z} - \mathbf{U}[\Psi^t]$ ,  $\boldsymbol{\omega} \sim \mathcal{N}(\mathbf{0}, \mathbf{Q})$ ;  $\mathbf{U} : \Psi \mapsto \mathbf{z}$ . Its likelihood is given by

$$p(\mathbf{z}|\Psi) \propto \exp\left\{-\underbrace{\frac{1}{2}(\mathbf{z} - \mathbf{U}[\Psi])^T \mathbf{Q}^{-1} (\mathbf{z} - \mathbf{U}[\Psi])}_{\mathcal{J}_z}\right\}. \quad (8)$$

If this static data  $\mathbf{z}$ , corresponds to coarse-scale permeability data [15,27], then  $\mathbf{U} = [\mathcal{U} \mathbf{0} \mathbf{0} \mathbf{0}]$ . Where  $\mathcal{U} : \boldsymbol{\kappa}_f \mapsto \boldsymbol{\kappa}_c$ , is a nonlinear mapping that maps the fine-scale permeability field ( $\boldsymbol{\kappa}_f$ ) to coarse-scale field ( $\boldsymbol{\kappa}_c$ ) via an upscaling procedure (e.g., [10,11]), details are provided in Section 3.1.

Now, our goal is to obtain an estimate which is based on both of the above dynamic and static data. The likelihood of  $\mathbf{y}$  is given by

$$p(\mathbf{y}|\Psi) \propto \exp\left\{-\underbrace{\frac{1}{2}(\mathbf{y} - \mathbf{H}[\Psi])^T \mathbf{R}^{-1} (\mathbf{y} - \mathbf{H}[\Psi])}_{\mathcal{J}_y}\right\}.$$

The probability distribution function (pdf) of the predicted ensemble,

$$p(\Psi) \propto \exp\left\{-\underbrace{\frac{1}{2}(\Psi - \overline{\Psi})^T (\mathbf{P}^f)^{-1} (\Psi - \overline{\Psi})}_{\mathcal{J}_f}\right\},$$

where  $\overline{\Psi}$  and  $\mathbf{P}^f$  are the predicted ensemble mean and covariance respectively (eqns. 5a–5b). Then, using Bayes theorem, we obtain

$$p(\Psi|\mathbf{z}, \mathbf{y}) = \frac{p(\Psi, \mathbf{z}, \mathbf{y})}{p(\mathbf{z}, \mathbf{y})} = \frac{p(\mathbf{z}, \mathbf{y}|\Psi) p(\Psi)}{p(\mathbf{z}, \mathbf{y})} \propto p(\mathbf{z}, \mathbf{y}|\Psi) p(\Psi) = p(\mathbf{z}|\Psi) \underbrace{p(\mathbf{y}|\Psi) p(\Psi)}_{\propto p(\Psi|\mathbf{y})}.$$

The last term in above equation implies that the two independent data,  $\mathbf{y}$  and  $\mathbf{z}$  can be sequentially assimilated in the following two steps. We first assimilate observation  $\mathbf{y}$  to obtain an intermediate ensemble,  $\{\widetilde{\Psi}^{(i)}\}_{i=1}^{N_e}$ , as discussed in Section 2.2.

$$p(\widetilde{\Psi}) = p(\Psi|\mathbf{y}) \propto \exp\{-(\mathcal{J}_f + \mathcal{J}_y)\}, \quad (9)$$

This intermediate ensemble and likelihood in eqn. (8), can then be combined to obtain the final estimate  $\{\widehat{\Psi}^{(i)}\}_{i=1}^{N_e}$ .

$$p(\widehat{\Psi}) = p(\Psi|\mathbf{z}, \mathbf{y}) \propto \exp\{-(\mathcal{J}_f + \mathcal{J}_y + \mathcal{J}_z)\}. \quad (10)$$

Therefore, in a least-squared sense, the final estimate maximizes the posterior pdf  $p(\Psi|\mathbf{z}, \mathbf{y})$ , which corresponds to the minimum of  $\mathcal{J} = \mathcal{J}_z + \mathcal{J}_y + \mathcal{J}_f$ . See Appendix A for further details (where we show that the solution  $\widehat{\Psi}^{(i)}$  corresponds to the minimum of  $\mathcal{J}$ , for any  $i^{\text{th}}$  ensemble member). The coarse-scale EnKF algorithm is detailed in Appendix B, and a flow chart is given in Fig. 2.

### 3.1 Upscaling methods

In brief, the main idea behind upscaling of absolute fine-scale permeability is to obtain effective coarse-scale permeability for each coarse-grid block. Once the upscaled absolute permeability is computed, the original equations are solved on the coarse-grid, without changing the form of relative permeability curves. This is an inexpensive calculation, since the pressure update involves only solving the pressure equation on the coarse-grid, and one can take larger time step for solving the transport equation. In our numerical simulations, the fine-grid is coarsened 10 times in each direction. These kinds of upscaling techniques in conjunction with the upscaling of absolute permeability have been used in groundwater applications (see e.g., [13,12,11]).

The link between the coarse and the fine-scale permeability fields is usually nontrivial because one needs to take into account the effects of all the scales present at the fine level. In the past simple arithmetic, harmonic or power averages have been used to link properties at various scales. These averages can be reasonable for low heterogeneities or for volumetric properties such as porosity. For permeabilities, simple averaging can lead to inaccurate and misleading results. In this paper we use the flow-based upscaling methods using local solutions of the equations [10,36].

First, we briefly describe flow based upscaling methods. Consider the fine-scale permeability that is defined in the domain with underlying fine grid as shown in Figure 1. On the same graph we illustrate a coarse-scale partition of the domain. To calculate the coarse-scale permeability field at this level we need to determine it for each coarse block,  $\Omega_c$ . The coarse block permeability can

be defined both using the solutions of local or global problems. The main idea used to calculate the coarse-scale permeability is that it should deliver the same average response as that of the underlying fine-scale problem, locally. The calculation of the coarse-scale permeability based on local solutions is schematically depicted in Figure 1. For each coarse domain  $\Omega_c$  we solve the local problems

$$\nabla \cdot (\boldsymbol{\kappa}_f(\mathbf{x}) \nabla \phi_j) = 0, \quad (11)$$

with some coarse-scale boundary conditions.

One of such boundary conditions is given by  $\phi_j = 1$  and  $\phi_j = 0$  on the opposite sides along the direction  $e_j$  and no flow boundary conditions on all other sides, alternatively,  $\phi_j = x_j$  on  $\partial\Omega_c$ . For these boundary conditions the coarse-scale permeability is given by

$$\boldsymbol{\kappa}_c \mathbf{e}_j \cdot \mathbf{e}_l = \frac{1}{|\Omega_c|} \int_{\Omega_c} \boldsymbol{\kappa}_f(\mathbf{x}) \nabla \phi_j \cdot \mathbf{e}_l dx, \quad (12)$$

where  $\phi_j$  is the solution of eqn. (11) with prescribed boundary conditions. Various boundary condition can have some influence on the accuracy of the calculations, including periodic, Dirichlet, etc. These issues have been discussed for e.g., in [36]. In particular, for determining the coarse-scale permeability field one can choose local domains that are larger than target coarse block,  $\Omega_c$ , for eqn. (11). Further eqn. (12) is used in the domain  $\Omega_c$ , where  $\phi_j$  are computed in the larger domains with correct scaling (see [36]). This way one reduces the effects of the artificial boundary conditions imposed on  $\Omega_c$  (for details see [36]).

The use of the local solutions eqn. (11) for determining the permeability field at different scales gives non-explicit relation for conditional distribution. We denote by  $\mathcal{U}$  the local operator that maps the local fine-scale permeability field  $\boldsymbol{\kappa}_f$  into  $\boldsymbol{\kappa}_c$ , defined as above. For our computations we assume

$$\boldsymbol{\kappa}_c = \mathcal{U}(\boldsymbol{\kappa}_f) + \epsilon, \quad (13)$$

where  $\epsilon$  are some random fluctuations that represent inaccuracies in the coarse-scale permeability. One of the sources of these fluctuations are the errors associated with solving inverse problems on the coarse grid. The other source of the inaccuracies of measured coarse-scale permeability is due to the fact that the inversion on the coarse grid does not take into account the adequate form of the coarse-scale models. Indeed, the inversion on the coarse grid for flow problems often involves the same flow equations as the underlying fine ones, for example, the same relative permeabilities are used for the coarse-scale problems as those for the fine scale problems or the effects of macrodispersion are neglected. It is known that [11,17–19] the flow equations at the coarse level may have different form from the underlying fine-scale equations. In general this form depends on the detailed nature of the heterogeneities which are very

difficult to obtain in solving inverse problems. Thus, calculating the coarse-grid permeability fields by matching the production history introduces some errors. We present an algorithm in Section 5, which attempts to model the relation between coarse- and fine-scale water cuts via a number of off-line fine and coarse simulations.

## 4 Numerical results

For our numerical tests with the coarse-scale EnKF algorithm, we use a  $50 \times 50$  fine grid (dimensionless domain size  $50 \times 50$ ) and two kinds of coarse-scale data. First we consider coarse-scale permeability, which could be obtained by coarse-scale inversion of fractional flow data on a coarse grid [15,37]. In Section 5, we discuss an alternative *sequential* coarse-scale inversion procedure to obtain coarse-scale permeability. This coarse-scale field could be thought as *static* data, which is to be honored as constraint (up to the data variance) in eqn. (8), hence we need to always assimilate it in our coarse-scale EnKF algorithm.

For the second set of results, coarse-scale saturation, can be considered as obtained from inversion of 4d seismic measurements (see Introduction, Section 1). Here, the coarse-grid saturation was obtained by volume averaging of true fine-scale saturation at some specific observation times (further details are given in Section 4.3). Therefore unlike coarse-scale permeability, static data constraint, which is to be always satisfied, the coarse-scale saturation data is assumed to be available at only a few observation times. Following the flowchart in Fig. 2 for the coarse-scale EnKF, we always have coarse-scale data if it is coarse permeability; and only at those few observation times for coarse-scale saturation data.

An initial ensemble with different permeability realizations was generated using the sequential Gaussian simulation (SGSIM)<sup>1</sup> [7]. We specified a Gaussian variogram model with a correlation length of 20 gridblocks in the x-direction and 5 gridblocks in the y-direction; one of the realizations is used as the reference field (depicted in Fig. 3). The fractional flow will be calculated based on the fine-scale model in Section 2.1. Porosity ( $\phi$ ) is assumed to be equal to 0.15 for all grid blocks. For simplicity, relative permeabilities,  $k_{rj}$  are assumed to be linear functions of water saturation ( $S$ ):  $k_{rw}(S) = S$ ,  $k_{ro}(S) = 1 - S$ . We note that this linearity assumption does not affect our data assimilation results. When single-phase upscaling (i.e., upscaling of absolute permeability only) is used, the errors in water cuts between coarse- and fine-scale simu-

---

<sup>1</sup> For reservoir simulation applications, the SGSIM has been used [23,8] for generating initial ensemble members. This approach yields independent and identically distributed multivariate normal random fields (conditioned to well log data)

lations behave similarly for linear and nonlinear relative permeabilities (with no extreme viscosity ratios) [12]. One injection well at the center of the field (injection rate:  $71.4 \text{ m}^3/\text{day}$ ) and four producing wells at the four corners (all with equal rate of  $17.85 \text{ m}^3/\text{day}$ ) were considered. The model equations are solved with no flow boundary conditions, zero initial water saturation, and discretizing the transport equation using first order upwind finite volume method. In Fig. 4, we provide the predicted fractional flow for 256 initial ensemble members along with the true fractional flow (obtained from true permeability field).

To compare our proposed coarse-scale constrained **EnKF** results with the regular **EnKF** we will use the following mean  $L_2$ -norm error. Since we know the true (fine and coarse-scale) field for our synthetic problem, i.e., the true permeability field, denoting it by  $\boldsymbol{\kappa}^{true}$ , the error for any ensemble member is

$$\mathbf{e}^{(i)} = \boldsymbol{\kappa}^{(i)} - \boldsymbol{\kappa}^{true}, \quad i = 1, 2, \dots, N_e.$$

Consider the  $L_2$  norm of the error for each member,  $\|\mathbf{e}^{(i)}\|_2 = \sqrt{\sum_j [\mathbf{e}_j^{(i)}]^2}$ , using which we define the mean  $L_2$  error as

$$\bar{\mathbf{e}} = \frac{1}{N_e} \sum_{i=1}^{N_e} \|\mathbf{e}^{(i)}\|_2, \quad (14)$$

so that  $\bar{\mathbf{e}}$  gives us an indication of the *distance* of entire ensemble from the true solution  $\boldsymbol{\kappa}^{true}$ . Since after every observation, we have updated ensemble members, therefore we can monitor the variation of  $\bar{\mathbf{e}}$  over the time of assimilation; the success of assimilation can therefore be related to the decrease in  $\bar{\mathbf{e}}$ .

#### 4.1 **EnKF** with fractional flow data only

We start with a presentation of results with *regular EnKF*, *assimilating only water cut data*. Next we will discuss results with the coarse-scale **EnKF**.

The water cut data from the reference field is assumed to be available every 200 days, with mean zero and standard deviation of 0.01 (therefore  $\mathbf{R}^{1/2} = 0.01\mathbf{I}_4$ , where  $\mathbf{I}_4$  is unit matrix of size  $4 \times 4$ , since there are four producing wells). The observed data is assumed to be available up to 2400 days, hence we will perform assimilation between 200 and 2400 days. A *prediction beyond interval of data assimilation, up to 4000 days* is also provided.

The choice of ensemble size ( $N_e$ ) is very important for successful data assimilation using **EnKF**. This is because a finite size ensemble prediction is used to estimate the prior error covariance,  $\mathbf{P}^f$  (eqn. 5b). For small sample sizes,

sampling errors in the covariance estimates result in insufficient variance for  $\mathbf{P}^f$ , so that observations which lie outside the small ensemble spread are completely ignored [5] (we are trying to sample a covariance matrix for unknown variables:  $\ln(\boldsymbol{\kappa})$ ,  $\mathbf{pr}$ ,  $\mathbf{S}$ ,  $\mathbf{W}_c$ , i.e., an unknown of size  $3 \times 2500$  plus four fractional flow data in this case, using sample sizes that are far lesser, resulting in severely reduced rank covariance matrices; see Fig. 5 for a plot of variance during assimilation for various ensemble sizes). Different approaches such as covariance inflation, localization, have been proposed to alleviate this problem of ensemble *inbreeding*, which are discussed elsewhere, see [1,26,25,2,8] for further details. Therefore we need to select a *sufficiently large* ensemble size, which would not severely suffer from the above described problem. Based on Fig. 5, we select an ensemble of size 256 for our data assimilation results, which has about 13% loss in variance.

We assimilated the above described measured data, and using the assimilated permeability field, in Fig. 6 we plot the assimilated water cut data along with the true data. Comparing with the initial forecast in Fig. 4, we observe that the assimilated ensemble better envelopes the true data. We compare the final permeability field after assimilation (Fig. 22(a)–22(d)) for a few ensemble members with the true field in Fig. 3 (also given are the initial values Fig. 21(a)–21(d)); note that the central, South East–North West channel is prominent but the features at the South West and North East corners are not well captured. Therefore assimilation of only water cut data helps in identifying only some of the important features.

#### 4.2 Coarse-scale constrained *EnKF* with fractional flow and coarse-scale permeability data

In addition to water cut production data, the coarse-scale permeability data, as described in Section 3.1 has been used as additional measured data. Flow-based upscaling of reference permeability field is used as a proxy for inverted coarse field (coarse-scale inversion was discussion in Section 3.1). Following our previous notation, this coarse-scale permeability data will be denoted by  $\mathbf{z}$  (eqn. 8). The mapping between state variables (at fine-scale) and observations (at coarse-scale) is given by  $\mathbf{U} = [\mathcal{U} \ \mathbf{0} \ \mathbf{0} \ \mathbf{0}]$ ,  $\mathcal{U}$ , denotes flow-based upscaling.

Exactly as in the previous section, we prescribed the same frequency (of availability) and precision,  $\mathbf{R}$  for the fractional flow data. Since we use coarse-scale permeability as additional data, it is to be assimilated whenever we assimilate water cut data. A  $5 \times 5$  coarse-scale data with mean zero and variance,  $\mathbf{Q} = q\mathbf{I}_{25}$  (we will present results with  $q = 4, 2, 1, 0.5$  and  $0.1$ ), so that we can consider the impact of coarse-scale data precision. In Fig. 7 we plot the variation of mean  $L_2$  error,  $\bar{e}$  (eqn. 14) with observation time, at the coarse-scale

for different values of  $q$ . Figures 8(a) and 8(b) depict the correlation between coarse-scale ensemble mean and true fields for  $q = 4$  and 0.1, respectively. As the precision of coarse-scale data is increased, i.e., for smaller variance, we observe a larger decrease in coarse-scale mean  $L_2$  error and higher correlation with true coarse-scale field (correlation coefficient for  $q = 4, 2, 1, 0.1$  respectively are 0.976, 0.992, 0.995, 0.999), because smaller variance  $\mathbf{Q}$  implies more stricter coarse-scale data constraint in eqn. (8). Fig. 9(a)–9(d) depict the fractional flow using the final permeability field after assimilation, for different coarse-scale data precisions. Fig. 7 and 8(a)–8(b) show that the coarse-scale data is being more accurately assimilated as it is made more precise. Also, notice the improved fit of ensemble prediction to the true data, for more precise coarse-scale data; also when compared to the regular EnKF results in Fig. 6.

Now we discuss the results regarding fine-scale field. In Fig. 10 we plot the fine-scale mean  $L_2$  error for different values of  $q$ ; the coarse-scale EnKF yields much lesser error than regular EnKF which assimilated only fractional flow data. The correlation coefficient between fine-scale ensemble mean and true fields, after assimilating using regular EnKF is equal to 0.409, while with the coarse-scale EnKF for  $q = 4, 2, 1, 0.1$ , in that order were 0.644, 0.652, 0.638, and 0.626; note higher correlation with the coarse-scale EnKF. We observe that higher precision, i.e., lower  $q$  does not necessarily imply least  $\bar{\epsilon}$  or highest correlation, since highly precise coarse-scale data is relatively more weighted than the fractional flow data. Optimal value for the coarse-scale data variance can be obtained by prior calculation, which will be addressed in a future study.

The final permeability field, for a few ensemble members after assimilating with coarse-scale EnKF, for  $q = 1$  is shown in figures 23(a)–23(d); all shown samples seem to be more closer to the true field (Fig. 3) than those obtained with regular EnKF (Fig. 22(a)–22(d)). In particular note that the low permeability region at the North East and high permeability at the South West corners are well captured.

#### *4.3 Coarse-scale constrained EnKF with fractional flow and coarse-scale saturation data*

As mentioned in the Introduction and Section 3.1, by coarse-scale inversion of 4d-seismic data, we could obtain dynamic data such as coarse-scale pressure and saturation. In this section we will use our proposed coarse-scale EnKF algorithm to study the impact of usage of coarse-scale saturation as measured data. To this end, the saturation obtained by using the reference permeability, is saved at three different times: 200, 1200 and 2400 days which correspond to the start, middle and end of the time window of data assimilation. This saved fine-scale saturation field is then upscaled (see Section 3.1) by volume averag-

ing to a  $5 \times 5$  coarse-scale grid and used as observed coarse-scale saturation data. If we denote the volume averaging by operator  $\mathcal{A}$ , acting on fine-scale saturation  $S_f$ , to give coarse-scale saturation  $S_c = \mathcal{A}S_f$ , then the mapping between state variables at fine-scale and measured data at coarse-scale is given by  $\mathbf{U} = [\mathbf{0} \ \mathbf{0} \ \mathcal{A} \ \mathbf{0}]$ . Therefore in Steps 2.1 and 2.4, of the coarse-scale EnKF algorithm (Appendix B), we use this operator to compute the misfit:  $\mathbf{z} - \mathbf{U}[\Psi]$ . Unlike the coarse-scale permeability data which is to be taken into account at every assimilation step, by construction, the coarse-scale saturation data is available only at a few assimilation steps, in this particular case, assimilation after 200, 1200 and 2400 days.

To be consistent with our previous results, the frequency (of availability) and precision,  $\mathbf{R}$  for the fractional flow data has been kept the same. The coarse-scale saturation data with mean zero and variance,  $\mathbf{Q} = q_s \mathbf{I}_{25}$  (we will consider results with  $q_s = 0.5, 0.1, 0.01$ ) such that the precision is varied from low- high. Since the saturation ranges between zero and one, and the fractional flow data is usually more accurately measured than 4d-seismic data, we picked  $q_s$  to be always larger than the variance in fractional flow data. In Fig.11 we plot the variation of mean  $L_2$  error for the coarse-scale saturation (while assimilating) versus observation time (for our test case, we had assumed zero initial water saturation, therefore the water saturation increases with time, hence the inherent, increasing trend in Fig. 11). Note that whenever the coarse-scale saturation is assimilated the error decreases for all three values of  $q_s$ . Once the data has been assimilated using the coarse-scale EnKF algorithm, we predict using the assimilated ensemble members. The correlation of predicted coarse-scale saturation with the true coarse-scale field at 200, 1200 and 2400 days, for different values of  $q_s$  is given in figures 12(a)–14(c); note the higher correlation for more precise coarse-scale data. The improved fit of the fractional flow data prediction using the assimilated ensemble members is given in Fig.15(a)–15(c). For less precise data, such as  $q_s = 0.5$  : Fig.15(a), the results are somewhat similar to the regular EnKF results (Fig. 6), but as the precision is increased ( $q_s = 0.01$ ) the coarse-scale EnKF prediction is certainly improved and is closer to the truth.

We discuss the fine-scale results, starting with fine-scale saturation and then the fine-scale permeability. The true fine-scale saturation at certain times, is plotted in Fig. 16(a)–16(g). The mean saturation with initial ensemble members (before data assimilation) is given in Fig. 17(a)–17(g) and Fig. 18(a)–18(g) show the field after assimilating only fractional flow data using regular EnKF. Using the coarse-scale EnKF, with  $q_s = 0.01$  is shown in Figures 19(a)–19(g). Note that we are able to capture many of the subtle features that are present in the true saturation field, such as the fingers that develop off the center toward the North East corner and sharp contrast between different levels of saturation, throughout the entire time interval (up to 4000 days) considered.

Next we discuss the fine-scale permeability results after assimilation with our coarse-scale **EnKF**. A comparison of the mean  $L_2$  error for the fine-scale permeability field for varying  $q_s$  and that obtained using the regular **EnKF** is shown in Fig. 20. Note that the error variation with  $q_s = 0.5$  is very close to that with regular **EnKF**, which probably explains why the fractional flow (Fig. 15(a)) is not much different from the assimilation of water cut data only (regular **EnKF**). Similarly improved results with  $q_s = 0.01$  could be explained based on smallest mean  $L_2$  error for the fine-scale permeability. Finally the fine-scale permeability field for a few ensemble members is plotted in Fig. 24(a)–24(d). Notice that though the South East– North West features are captured, unlike the results obtained with coarse-scale permeability data (Fig. 23(a)– 23(d)), the South West and North East features are not well represented. In general the results with coarse-scale permeability data are better, in terms of fine-scale mean  $L_2$  error decrease and permeability samples, when compared to usage coarse-scale saturation data, which is anticipated, since the fine scale permeability is more correlated to coarse-scale permeability than coarse-scale saturation. Also, these results highlight the importance of accurate coarse-scale data and modeling, since more accurate measurements lead to further decrease in uncertainty at the fine-scale.

## 5 Coarse-Scale Inversion

We assume that the observed water cut data corresponds to the model’s finest scale response. This relationship will be written as,

$$y_f^o(t_n) = \mathcal{M}_f(t_n)[\boldsymbol{\kappa}_f^{true}], \quad (15)$$

where  $y_f^o(t_n)$  is the observed water cut, superscript ‘ $o$ ’ denotes observed data, subscript ‘ $f$ ’, fine-scale and  $t_n$ , the time step. The fine-scale model and *true* permeability are respectively denoted by  $\mathcal{M}_f$  and  $\boldsymbol{\kappa}_f^{true}$ . Once  $\boldsymbol{\kappa}_f^{true}$  is upscaled, we get  $\boldsymbol{\kappa}_c^{true}$ , which could be used to obtain the so-called coarse-scale water cut,

$$y_c^*(t_n) = \mathcal{M}_c(t_n)[\boldsymbol{\kappa}_c^{true}], \quad (16)$$

using the coarse-scale model,  $\mathcal{M}_c$ . Hence to obtain the coarse-scale *true* permeability,  $\boldsymbol{\kappa}_c^{true}$ , we first need to generate coarse-scale water cut data that corresponds to the reference fine-scale water cut. This coarse-scale data could then be inverted to obtain the coarse-scale field, for e.g., using coarse-scale gradient sensitivity [37]; here we will instead use regular **EnKF** algorithm on a coarse-grid and, sequentially estimate the coarse-scale permeability field. The assimilated coarse-scale ensemble mean permeability obtained after a certain number of days could then be used as a constraint for coarse-scale **EnKF** described in section 4.2. In other words, this methodology could be used to obtain coarse-scale permeability data, using the observed water cut data, say

between time:  $[t_1, t_2]$ ,  $0 < t_1 < t_2$ . Then we can use coarse-scale permeability and observed water cut within  $(t_2, T]$ , for coarse-scale EnKF (the final water cut observation is at time,  $T$ ). However, the first step is to obtain the coarse-scale production data (which will be denoted by  $\tilde{y}_c(t_n)$ ) using the observed fine-scale data,  $y_f^o(t_n)$ .

### 5.1 Fine-scale to coarse-scale production map

Using an ensemble of fine-scale fields:  $\boldsymbol{\kappa}_f^{(i)}, i = 1, N_e$ , we obtain corresponding fine-scale water cut,  $y_f^{(i)}(t_n) = \mathcal{M}_f(t_n)[\boldsymbol{\kappa}_f^{(i)}]$ . By single phase flow based upscaling of fine-scale ensemble permeability fields we obtain,  $\boldsymbol{\kappa}_c^{(i)}, i = 1, N_e$ . Therefore using the coarse-scale model, we get  $y_c^{(i)}(t_n) = \mathcal{M}_c(t_n)[\boldsymbol{\kappa}_c^{(i)}]$ , such that at any time step,  $t_n$ , for every fine-scale fractional flow data value, there is a corresponding coarse-scale image point. In Fig. 25, we plot for an arbitrary ensemble member the fine and coarse-scale fractional flow curves, with the same configuration of wells as earlier including the fine and coarse-scale grid sizes, namely,  $50 \times 50$  and  $5 \times 5$  respectively. A plot of fine-scale versus coarse-scale water cut for one of the four producers at the end of 3000 days is shown in Fig. 26 with  $N_e = 100$  realizations. Given the discrete sets:  $\{y_f^{(i)}(t_n)\}$  and  $\{y_c^{(i)}(t_n)\}$ , here we adopt a simple linear least-squares approach to obtain coarse-scale water cut,  $\tilde{y}_c(t_n)$  corresponding to observed fine scale data,  $y_f^o(t_n)$ . We start by writing any coarse-scale fractional flow value as,

$$y_c^{(i)}(t_n) = \alpha(t_n)y_f^{(i)}(t_n) + \beta(t_n), \quad (17)$$

where  $\alpha(t_n)$  and  $\beta(t_n)$  are scalar coefficients. Least-squares fit values ( $\alpha^*(t_n)$  and  $\beta^*(t_n)$ ) of these parameters are obtained by minimizing,

$$\sum_{i=1}^{N_e} (y_c^{(i)} - \alpha y_f^{(i)} - \beta)^2$$

at every  $t_n$  (a similar approach was studied by Omre and Løvdøen [33] to model a mapping of coarse-scale to fine-scale water cut). Therefore  $\tilde{y}_c(t_n) = \alpha^*(t_n)y_f^o(t_n) + \beta^*(t_n)$  and, could be seen as an approximation to  $y_c^*(t_n)$ , the true coarse-scale water cut (eqn.16). This off-line method therefore relies on a number of fine and coarse-scale simulations. As mentioned in section 2.1, coarse-scale simulation is relatively inexpensive when compared to the computational cost of a corresponding fine-scale simulation and since this entire procedure can be implemented offline, it is affordable. Moreover, for our results we map the observed fractional flow only in the early time period, to obtain  $\tilde{y}_c$ . The same fine-scale reference field as earlier in Section 4 (Fig. 3), when upscaled (flow based) yields coarse-scale field, when used in coarse-scale simulation provides  $y_c^*$ . The observed fractional flow data,  $y_f^o$ , is also the same as used earlier,

for e.g., in regular **EnKF**, Section 4.1. A comparison of  $\tilde{y}_c$  (obtained from above described mapping of  $y_f^o$ ) and  $y_c^*$  is given in Fig. 27. The mapped coarse-scale fractional flow,  $\tilde{y}_c$  deviates slightly from  $y_c^*$ , however, this could be minimized by considering a larger sample size and/or a different fit other than the linear fit, to be studied in future research work.

## 5.2 *EnKF on coarse-grid*

Our goal is to sequentially estimate coarse-scale state (including coarse-scale permeability) using the above obtained coarse-scale water cut. The regular **EnKF** algorithm is implemented for the coarse-scale permeability samples,  $\kappa_c^{(i)}, i = 1, N_e$  and  $\tilde{y}_c$ , as coarse-scale *observed* data. This can be accomplished with minimal computational resources since the size of the coarse-grid is relatively much smaller than the fine-scale grid. Because upscaled permeability fields are used for imposing a constraint in **EnKF**, we can also use MCMC techniques (e.g., [16]) to obtain coarse-scale permeability samples conditioned to water-cut data. In Fig. 28 we compare the assimilated coarse-scale ensemble mean permeability with the reference coarse-scale field (flow upscaled fine-scale permeability). We observed that the ensemble mean coarse-scale permeability after coarse grid data assimilation, is approximately the same as coarse-scale permeability field obtained by flow-based upscaling of the fine-scale reference permeability field. As a result, we observed that coarse-scale **EnKF** gives similar results to those presented earlier (in Section 4.2), which used flow-based upscaling of the fine-scale reference permeability field.

## 6 Conclusions

The **EnKF** is increasingly being used for subsurface characterization in various geological and groundwater applications to identify fine-scale state and parameters. So far, various implementations have been based on using dynamic, production data, such as water cut, well pressures, etc, for sequential data assimilation. Only recently dynamic data other than production data has been considered in the **EnKF** context ([9,34]), nevertheless the observed data to be assimilated was assumed to be at the finest scale. For a number of reasons, it is widely recognized that usage of additional multiscale data could further reduce the uncertainty at the fine scale. This is further motivated by the increasing popularity of coarse-scale modeling. In this light, here we proposed assimilation of coarse-scale data along with water cut, production data using *coarse-scale EnKF*. The modification to the regular **EnKF** (assimilation of only water cut data) is completely recursive and easily implementable. The relation between fine and coarse scales has been modeled via physics based

upscaling, which could be thought of as a nonlinear observation operator linking the coarse-scale data to the unknown fine-scale variables. In addition, the proposed methodology could be used in any other sequential data assimilation method as well.

The coarse-scale **EnKF** was tested and compared with the regular **EnKF** for a 2D synthetic  $50 \times 50$  heterogeneous true field. Two kinds of coarse-scale data were considered. In the first implementation, coarse-scale permeability data was considered. In the second, we considered volume averaged coarse-scale saturation from the reference case as coarse-scale data; in both cases, a  $5 \times 5$  coarse grid was used. The coarse-scale saturation was assimilated only three times in the entire time window of data assimilation (beginning, middle and end). Therefore unlike coarse-scale permeability data which was always assimilated along with water cut data, coarse-scale saturation was only thrice assimilated. The data variance was varied from low to high, to study its impact on assimilated results. In all cases, we observed that the assimilated, ensemble mean coarse-scale field for all variances was highly correlated to the true coarse-scale field. In addition, lower variance in the coarse-scale data yielded higher correlation. The water cut data was better honored, both for higher precision of coarse data, and when compared with regular **EnKF**. As for the fine-scale permeability field, the coarse-scale **EnKF** yielded lesser error in an averaged  $L_2$  norm, error taken w.r.t. the reference field. In addition, a few individual samples were picked to compare the assimilated fields with different **EnKF** procedures; experiment with coarse-scale permeability data provided final samples which captured most closely the features in the reference fine-scale field. We also compared the fine-scale water saturation profile for different times, a comparison with the regular **EnKF** showed that the profile with coarse-scale **EnKF** (with coarse saturation) replicated many of the subtle features present in the true saturation profile.

Though in our current paper we used only one coarse-scale, the proposed method can be easily implemented to integrate as many scales as required by the available data. We also discussed an alternative method to obtain coarse-scale permeability data, if it was not available from prior geological consideration. This procedure was based on first modeling an approximate relationship between fine- and coarse-scale fractional flows. The mapped coarse-scale fractional flow was then used in sequential estimation of coarse-scale permeability. Our results indicated that the estimated coarse-scale ensemble mean permeability is similar to the one obtained via a flow-based upscaling of the fine-scale reference field.

Our current and future work is directed toward assimilating observations at multiple scales into three dimensional models.

## **APPENDIX A Two step coarse-scale constrained Kalman filter es-**

**imate**

From Section 3,

$$\mathcal{J}_f = \frac{1}{2}(\Psi - \bar{\Psi})^T (\mathbf{P}^f)^{-1} (\Psi - \bar{\Psi}),$$

and

$$\mathcal{J}_y = \frac{1}{2}(\mathbf{y} - \mathbf{H}[\Psi])^T \mathbf{R}^{-1} (\mathbf{y} - \mathbf{H}[\Psi]).$$

For notational simplicity we will denote  $\mu_{\Psi}$  as  $\mu$  and denote  $\mathbf{P}^f$  by  $\mathbf{B}$ .

**Step 1** (minimize  $\mathcal{J}_f + \mathcal{J}_y$ ):

First we minimize the sum,  $\mathcal{J}_1 = \mathcal{J}_f + \mathcal{J}_y$ . The gradient<sup>2</sup> of above quadratic cost functional with respect to (w.r.t.)  $\Psi$  is given by

$$\nabla_{\Psi} \mathcal{J}_1 = \mathbf{B}^{-1} (\Psi - \mu) - \mathbf{H}^T \mathbf{R}^{-1} (\mathbf{y} - \mathbf{H}[\Psi]).$$

Then the minimizer  $\tilde{\mu}$ , of  $\mathcal{J}_1$  satisfies (we assume  $\mathbf{H}$  to be linear)

$$\mathbf{B}^{-1} (\tilde{\mu} - \mu) - \mathbf{H}^T \mathbf{R}^{-1} (\mathbf{y} - \mathbf{H}\tilde{\mu}) = 0.$$

Rearranging the above equation we get,

$$[\mathbf{B}^{-1} + \mathbf{H}^T \mathbf{R}^{-1} \mathbf{H}] \tilde{\mu} = \mathbf{B}^{-1} \mu + \mathbf{H}^T \mathbf{R}^{-1} \mathbf{y}. \quad (18)$$

Note that the Hessian of  $\mathcal{J}_1$  w.r.t.  $\Psi$  is given by  $\mathbf{B}^{-1} + \mathbf{H}^T \mathbf{R}^{-1} \mathbf{H}$ , and for linear quadratic cost functionals, the Hessian inverse is equal to the error covariance matrix. Therefore the error covariance matrix,  $\tilde{\mathbf{B}}$  for  $\tilde{\mu}$  is given by

$$\tilde{\mathbf{B}} = [\mathbf{B}^{-1} + \mathbf{H}^T \mathbf{R}^{-1} \mathbf{H}]^{-1}. \quad (19)$$

**Step 2** (minimize  $\mathcal{J}_g + \mathcal{J}_z$ ):

We use  $\tilde{\mu}$ ,  $\tilde{\mathbf{B}}$  in

$$\begin{aligned} \mathcal{J}_g &= \frac{1}{2}(\Psi - \tilde{\mu})^T (\tilde{\mathbf{B}})^{-1} (\Psi - \tilde{\mu}). \\ \mathcal{J}_z &= \frac{1}{2}(\mathbf{z} - \mathbf{U}[\Psi])^T \mathbf{Q}^{-1} (\mathbf{z} - \mathbf{U}[\Psi]). \end{aligned}$$

Therefore the minimum  $\hat{\mu}$ , of  $\mathcal{J}_g + \mathcal{J}_z$  satisfies

$$[(\tilde{\mathbf{B}})^{-1} + \mathbf{U}^T \mathbf{Q}^{-1} \mathbf{U}] \hat{\mu} = (\tilde{\mathbf{B}})^{-1} \tilde{\mu} + \mathbf{U}^T \mathbf{Q}^{-1} \mathbf{z}.$$

<sup>2</sup> We note in passing that  $\mathbf{B}$  and  $\mathbf{R}$  are covariance matrices and are positive definite by construction, and hence for our derivation purposes, are formally invertible.

Using equations (19) and (18) we can rewrite above as

$$\underbrace{[\mathbf{B}^{-1} + \mathbf{H}^T \mathbf{R}^{-1} \mathbf{H}] + \mathbf{U}^T \mathbf{Q}^{-1} \mathbf{U}}_{(\tilde{\mathbf{B}})^{-1}} \hat{\boldsymbol{\mu}} = \underbrace{\mathbf{B}^{-1} \boldsymbol{\mu} + \mathbf{H}^T \mathbf{R}^{-1} \mathbf{y}}_{r.h.s. \text{ of eqn. (18)}} + \mathbf{U}^T \mathbf{Q}^{-1} \mathbf{z}.$$

It is trivial to show that  $\hat{\boldsymbol{\mu}}$  also satisfies

$$\nabla_{\Psi} [\mathcal{J}_f + \mathcal{J}_y + \mathcal{J}_z] = 0.$$

Therefore the two step method to obtain the final estimate  $\hat{\boldsymbol{\mu}}$ , gives the same results as a one shot approach of minimizing  $\mathcal{J}_f + \mathcal{J}_y + \mathcal{J}_z$ .

## APPENDIX B The coarse-scale EnKF algorithm

---

**Algorithm 1** Coarse-scale EnKF algorithm
 

---

Run the simulation model up to a particular observation time for entire ensemble

to get predicted samples:  $\{\Psi^{(i)}\}_{i=1}^{N_e}$ ,  $\mathbf{A} = (\Psi^{(1)}, \Psi^{(2)}, \dots, \Psi^{(N_e)})$ .

- Step 1: Using measured water cut data  $\mathbf{y}$  with variance  $\mathbf{R}$ , get updated ensemble:  $\{\widetilde{\Psi}^{(i)}\}_{i=1}^{N_e}$ .

- Step 1.1 Find ensemble mean (eqn. 5a),  $\overline{\Psi}$ .

- Step 1.2 Subtract deviation from mean  $\mathbf{A}' = (\mathbf{b}^{(1)}, \mathbf{b}^{(2)}, \dots, \mathbf{b}^{(N_e)})$ ,  $\mathbf{b}^{(i)} = \Psi^{(i)} - \overline{\Psi}$ .

- Step 1.3 Apply  $\mathbf{H}$  to each column of  $\mathbf{A}'$  to get  $\mathbf{S} = \mathbf{H} \mathbf{A}'$ . i.e., simply pick the water cut deviations in  $\mathbf{A}'$ .

- Step 1.4 *for*  $i = 1, 2, \dots, N_e$ ,

Sample  $\boldsymbol{\nu}^{(i)} \stackrel{\text{i.i.d.}}{\sim} \mathcal{N}(\mathbf{0}, \mathbf{R})$ .

$\mathbf{y}^{(i)} = \mathbf{y} + \boldsymbol{\nu}^{(i)}$ ,

$\mathbf{R}^{1/2} = (\boldsymbol{\nu}^{(1)}, \boldsymbol{\nu}^{(2)}, \dots, \boldsymbol{\nu}^{(N_e)})$ ,

$\mathbf{D} = (\mathbf{d}^{(1)}, \mathbf{d}^{(2)}, \dots, \mathbf{d}^{(N_e)})$ ,  $\mathbf{d}^{(i)} = \mathbf{y}^{(i)} - \mathbf{W}_c^{(i)}$ ;  $\mathbf{W}_c^{(i)}$  is predicted water cut for each ensemble member.

*end for*

- Step 1.5 Compute SVD  $[\mathbf{S} + \mathbf{R}^{1/2}] = \mathbf{X}_L \Sigma \mathbf{X}_R$ .

Get  $\hat{\Sigma}$  retaining first few singular values which explain most variability in  $\Sigma$ , corresponding left singular vectors:  $\hat{\mathbf{X}}_L$ .

- Step 1.6 Update ensemble: eqn. (7),  $\widetilde{\mathbf{A}} = (\widetilde{\Psi}^{(1)}, \widetilde{\Psi}^{(2)}, \dots, \widetilde{\Psi}^{(N_e)})$ ,

$$\widetilde{\mathbf{A}} = \mathbf{A} + \mathbf{A}' \mathbf{S}^T \hat{\mathbf{X}}_L \hat{\Sigma}^{-2} \hat{\mathbf{X}}_L^T \mathbf{D}.$$

- Step 2: Using coarse-scale data  $\mathbf{z}$  with variance  $\mathbf{Q}$ , get updated ensemble:  $\{\widehat{\Psi}^{(i)}\}_{i=1}^{N_e}$ .

- Step 2.1 Compute coarse-scale ensemble prediction:  $\mathbf{u}^{(i)} = \mathbf{U} \widetilde{\Psi}^{(i)}$ ,  $i = 1, 2, \dots, N_e$ .

- Step 2.2 Coarse-scale mean:  $\boldsymbol{\mu}' = \frac{1}{N_e} \sum_{i=1}^{N_e} \mathbf{u}^{(i)}$ .

- Step 2.3 Coarse-scale deviations:  $\mathbf{S}' = (\mathbf{s}^{(1)}, \mathbf{s}^{(2)}, \dots, \mathbf{s}^{(N_e)})$ ,  $\mathbf{s}^{(i)} = \mathbf{u}^{(i)} - \boldsymbol{\mu}'$ .

- Step 2.4 Repeat Step 1.4, using coarse-scale measurement. *for*  $i = 1, 2, \dots, N_e$ ,

Sample  $\boldsymbol{\omega}^{(i)} \stackrel{\text{i.i.d.}}{\sim} \mathcal{N}(\mathbf{0}, \mathbf{Q})$ .

$\mathbf{z}^{(i)} = \mathbf{z} + \boldsymbol{\omega}^{(i)}$ ,

$\mathbf{Q}^{1/2} = (\boldsymbol{\omega}^{(1)}, \boldsymbol{\omega}^{(2)}, \dots, \boldsymbol{\omega}^{(N_e)})$ ,

$\mathbf{D}' = (\mathbf{d}^{(1)}, \mathbf{d}^{(2)}, \dots, \mathbf{d}^{(N_e)})$ ,  $\mathbf{d}^{(i)} = \mathbf{z}^{(i)} - \mathbf{u}^{(i)}$ .

*end for*

- Step 2.5 Compute SVD  $[\mathbf{S}' + \mathbf{Q}^{1/2}] = \mathbf{X}_L \Sigma \mathbf{X}_R$ . Get  $\hat{\Sigma}$  and  $\hat{\mathbf{X}}_L$  as in step 1.5

- Step 2.6 Compute fine-scale mean:  $\boldsymbol{\mu} = \frac{1}{N_e} \sum_{i=1}^{N_e} \widetilde{\Psi}^{(i)}$ .

- Step 2.7 Compute fine-scale deviations:  $\mathbf{A}'' = (\mathbf{b}^{(1)}, \mathbf{b}^{(2)}, \dots, \mathbf{b}^{(N_e)})$ ,  $\mathbf{b}^{(i)} = \widetilde{\Psi}^{(i)} - \boldsymbol{\mu}$ .

- Step 2.8 Update ensemble:  $\widehat{\mathbf{A}} = (\widehat{\Psi}^{(1)}, \widehat{\Psi}^{(2)}, \dots, \widehat{\Psi}^{(N_e)})$ ,

$$\widehat{\mathbf{A}} = \widetilde{\mathbf{A}} + (\mathbf{A}'')(\mathbf{S}')^T \hat{\mathbf{X}}_L \hat{\Sigma}^{-2} \hat{\mathbf{X}}_L^T \mathbf{D}'.$$


---

**Remark 1:**

Note that steps 2.6 and 2.7 in above algorithm approximate the intermediate fine-scale error covariance

$$\widetilde{\mathbf{P}}^f \approx \frac{1}{N_e - 1} \mathbf{A}'' (\mathbf{A}'')^T.$$

**Remark 2:**

Steps 2.1– 2.3 accomplish<sup>3</sup>

$$\mathbf{S}' = \mathbf{U} \mathbf{A}''.$$

Note that the above algorithm is independent of the choice of upscaling procedure and also, we can use the same algorithm for different kinds of coarse-scale observed data (if available).

**Remark 3:**

Note that the above coarse-scale constrained EnKF algorithm can be readily extended to incorporate data at multiple coarse scales, with appropriate upscaling procedure in  $\mathbf{U}$ . To elaborate, if we had another independent data at a scale different from  $\mathbf{z}$ , we use the estimates  $(\{\widehat{\Psi}^{(i)}\}_{i=1}^{N_e})$  obtained using  $\mathbf{z}$ , as intermediate solution, repeat Step 2 to assimilate the data at another scale.

**References**

- [1] Anderson JL. Exploring the need for localization in ensemble data assimilation using a hierarchical ensemble filter. *Physica D* 2007; 230(1-2): 99–111.
- [2] Arroyo-Negrete E, Devegowda D, Datta-Gupta A, Choe J. Continuous reservoir model updating using streamline assisted ensemble Kalman filter. *SPE Annual Technical Conference and Exhibition*, 24-27 September 2006, San Antonio, Texas, USA; 106518-STU.
- [3] Barker JW, Thibeau S. A critical review of the use of pseudo-relative permeabilities for upscaling, *SPE Res. Eng.* 1997; 12: 138–143.
- [4] Burgers G, van Leeuwen PJ, Evensen G. Analysis scheme in the ensemble Kalman filter. *Monthly Weather Review* 1998; 126(6): 1719–1724.
- [5] Chen Y, Zhang D. Data assimilation for transient flow in geologic formations via ensemble Kalman filter. *Advances in Water Resources* 2006; 29: 1107–1122.
- [6] Christie M. Upscaling for reservoir simulation. *J. Pet. Tech.* 1996; 1004–1010.
- [7] Deutsch CV, Journel A. *GSLIB Geostatistical Software Library and User's Guide*. Oxford Univ. Press, 1992.

<sup>3</sup> As noted in [21], this approach of accounting for nonlinear observations operator  $\mathbf{U}$ , works well, as long as  $\mathbf{U}$  is weakly nonlinear and a monotonic function of model variables  $\Psi$

- [8] Devegowda D, Arroyo-Negrete E, Datta-Gupta A. Efficient and robust reservoir model updating using ensemble Kalman filter with sensitivity-based covariance localization. SPE Reservoir Simulation Symposium held in Houston, TX, 26-28 February 2007; 106144-MS.
- [9] Dong Y, Gu Y, Oliver DS. Sequential assimilation of 4D seismic data for reservoir description using the ensemble kalman filter. Journal of Petroleum Science and Engineering 2006; 53: 83- 99.
- [10] Durlofsky LJ. Numerical calculation of equivalent grid block permeability tensors for heterogeneous porous media. Water Resour. Res. 1991; 27: 699–708.
- [11] Durlofsky LJ. Coarse scale models of two phase flow in heterogeneous reservoirs: Volume averaged equations and their relationship to the existing upscaling techniques. Computational Geosciences 1998; 2: 73–92.
- [12] Durlofsky LJ, Behrens RA, Jones RC, Bernath A. Scale up of heterogeneous three dimensional reservoir descriptions. SPE paper 30709, 1996.
- [13] Durlofsky LJ, Jones RC, Milliken WJ. A nonuniform coarsening approach for the scale up of displacement processes in heterogeneous media. Advances in Water Resources 1997; 20: 335–347.
- [14] Efendiev Y, Datta-Gupta A, Ginting V, Ma X, Mallick B. An efficient two-stage Markov chain Monte Carlo method for dynamic data integration. Water Resources Research 2005; 41: W12423.
- [15] Efendiev Y, Datta-Gupta A, Osako I, Mallick B. Multiscale data integration using coarse-scale models. Advances in Water Resources 2005; 28:303- 314.
- [16] Efendiev Y, Datta-Gupta A, Ginting V, Ma X, Mallick B. An efficient two-stage Markov chain Monte Carlo methods for dynamic data integration. Water Resources Research, 41, W12423, doi:=10.1029/2004WR003764
- [17] Efendiev Y, Durlofsky L. Generalized convection-diffusion model for subgrid transport in porous media. SIAM Multiscale Modeling and Simulation 2003; 1: 504526.
- [18] Efendiev Y, Durlofsky L. Accurate subgrid models for two-phase flow in heterogeneous reservoirs. SPE Journal 2004; 9: 219-226.
- [19] Efendiev YR, Durlofsky LJ. Numerical modeling of subgrid heterogeneity in two phase flow simulations. Water Resour. Res. 2002; 38(8): W1128.
- [20] Evensen G. Sequential data assimilation with a nonlinear quasi-geostrophic model using Monte Carlo methods to forecast error statistics. Journal of Geophysical Research 1994; 99(10), 14310, 162.
- [21] Evensen G. *Data Assimilation: The Ensemble Kalman Filter*. Springer, 2006.
- [22] Gosselin O, Aanonsen SI, Aavatsmark I, Cominelli A, Gonard R, Kolasinski M, Ferdinandi F, Kovacic L, Neylon K. History matching using time-lapse seismic (HUTS). SPE Annual Technical Conference and Exhibition, Denver 58 October 2003; SPE 84464-MS.

- [23] Gu Y, Oliver DS. History Matching of the PUNQ-S3 reservoir model using the ensemble Kalman filter. *SPE Journal* 2005; 10: 217- 224.
- [24] Gu YQ, Oliver DS. The ensemble kalman filter for continuous updating of reservoir simulation models. *Journal of Energy Resources Technology-Transactions of the ASME* 2006; 128: 79- 87.
- [25] Hamill T, Whitaker J, Snyder C. Distance-Dependent filtering of background error covariance estimates in ensemble Kalman filter. *Monthly Weather Review* 2001; 129: 2776- 2790.
- [26] Houtekamer P, Mitchell H. A sequential ensemble kalman filter for atmospheric data assimilation. *Monthly Weather Review* 2001; 129: 123-137.
- [27] Lee SH, Malallah A, Datta-Gupta A, Higdon D. Multiscale data integration using Markov random fields. *SPE Reservoir Evaluation Engineering* 2002; 5(1): 68- 78.
- [28] Lewis JM, Lakshmivarahan S, Dhall S. *Dynamic Data Assimilation: A Least Squares Approach (Encyclopedia of Mathematics and its Applications)*. Cambridge University Press, 2006.
- [29] Liu Y, Gupta HV. Uncertainty in hydrologic modeling: Toward an integrated data assimilation framework. *Water Resources Research* 2007; 43: W07401.
- [30] Lumley DE. Time-lapse seismic reservoir monitoring. *Geophysics* 2001; 66: 50-53.
- [31] Moradkhani H, Sorooshian S, Gupta H, Houser PR. Dual stateparameter estimation of hydrological models using ensemble Kalman filter. *Advances in Water Resources* 2005; 28: 135- 147.
- [32] Nævdal G, Johnson L, Aanonsen S, Vefring E. Reservoir monitoring and continuous model updating using ensemble Kalman filter. *SPE Journal* 2005; 10: 66- 74.
- [33] Omre H, Lødøen OP. Improved production forecasts and history matching using approximate fluid-flow simulators. *SPE Journal* 2004; 9: 339– 351.
- [34] Skjervheim J.-A, Evensen G, Aanonsen S, Ruud B, Johansen T. Incorporating 4D seismic data in reservoir simulation models using ensemble Kalman filter. *SPE Journal* 2007; 12: 282- 292.
- [35] Wen X.-H, Chen WH. Real-time reservoir model updating using ensemble Kalman filter. *SPE Reservoir Simulation Symposium* 2005; SPE 92991.
- [36] Wu XH, Efendiev YR, Hou TY. Analysis of upscaling absolute permeability. *Discrete and Continuous Dynamical Systems, Series B* 2002; 2: 185– 204.
- [37] Yoon S, Malallah AH, Datta-Gupta A, Vasco DW, Behrens RA. A Multiscale approach to production-data integration using streamline models. *SPE Journal* 2001; 6: 182– 192.

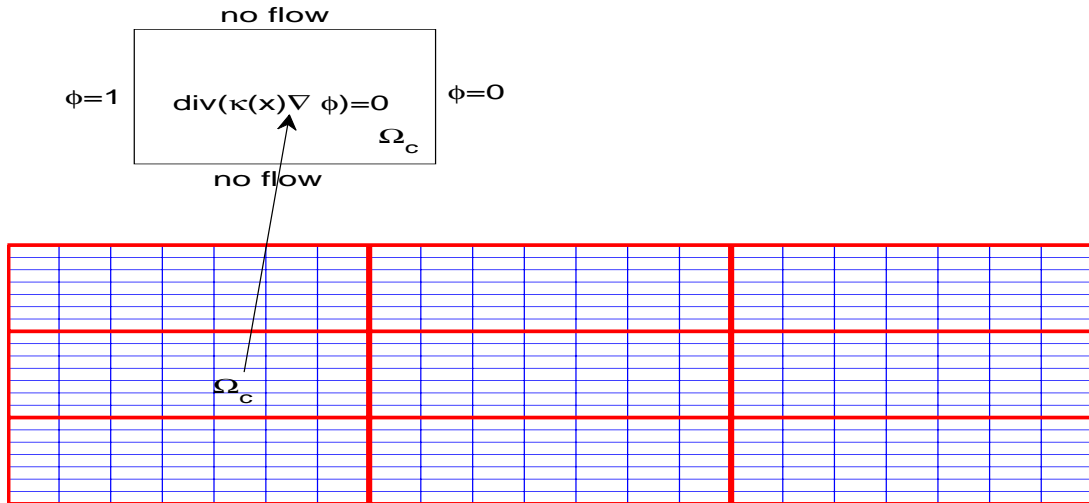


Fig. 1. Schematic description of the upscaling. Bold lines illustrate a coarse-scale partitioning, while thin lines show a fine-scale partitioning within coarse-grid cells.

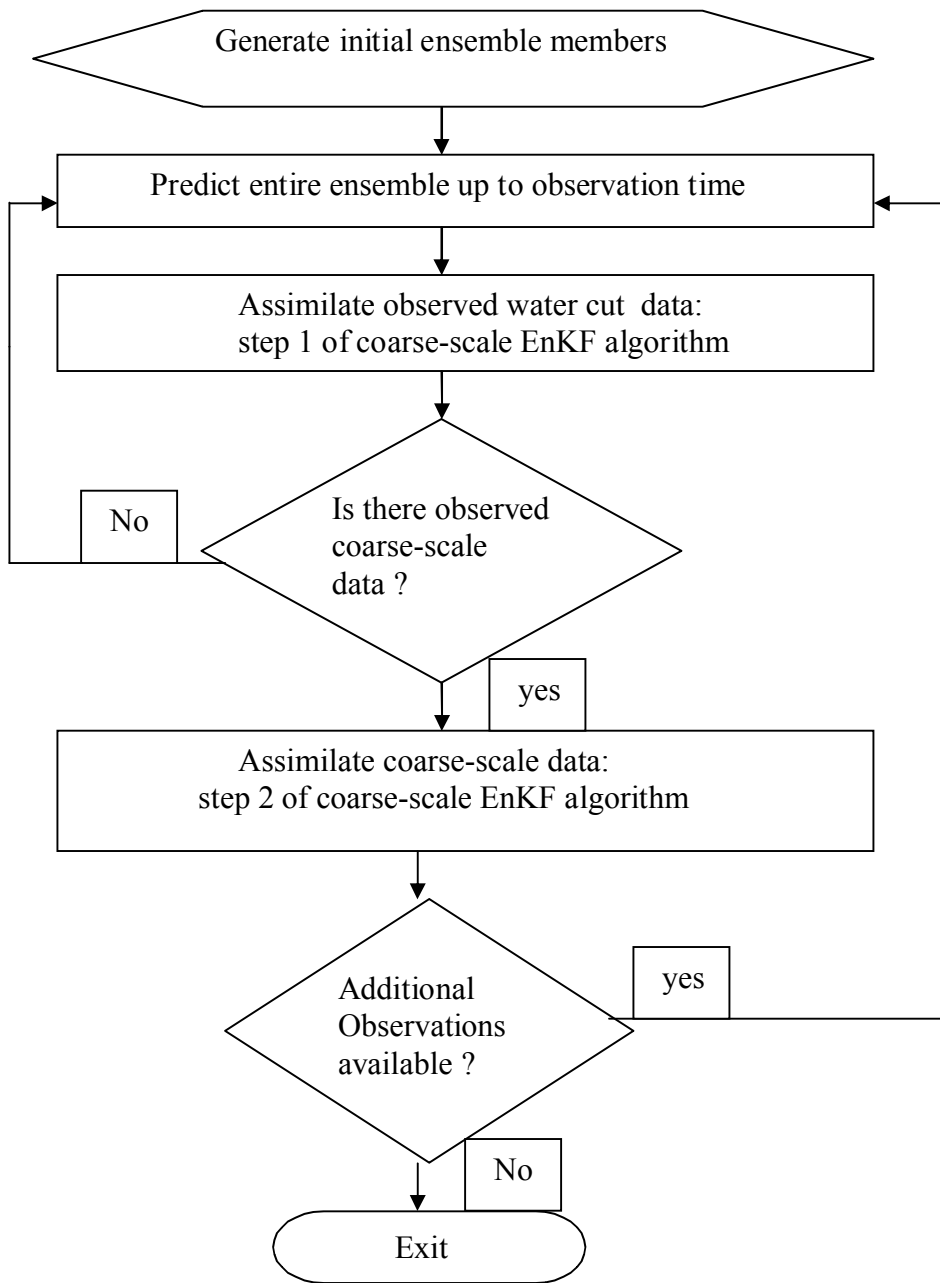


Fig. 2. Coarse-scale EnKF algorithm

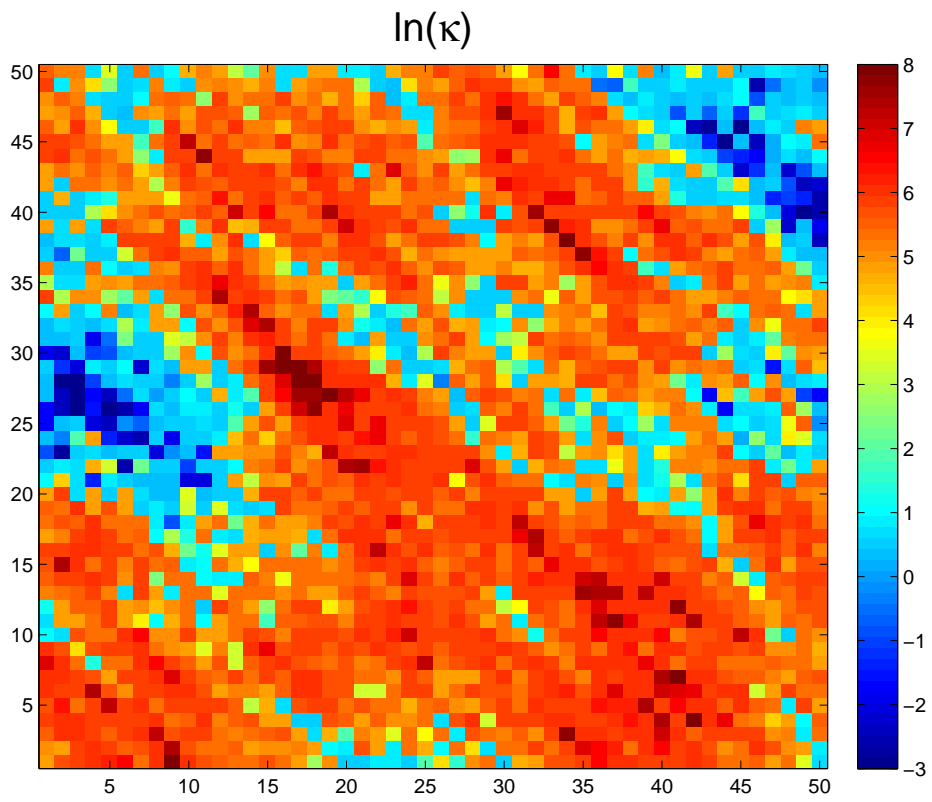


Fig. 3. Natural logarithm of  $50 \times 50$  true permeability field.

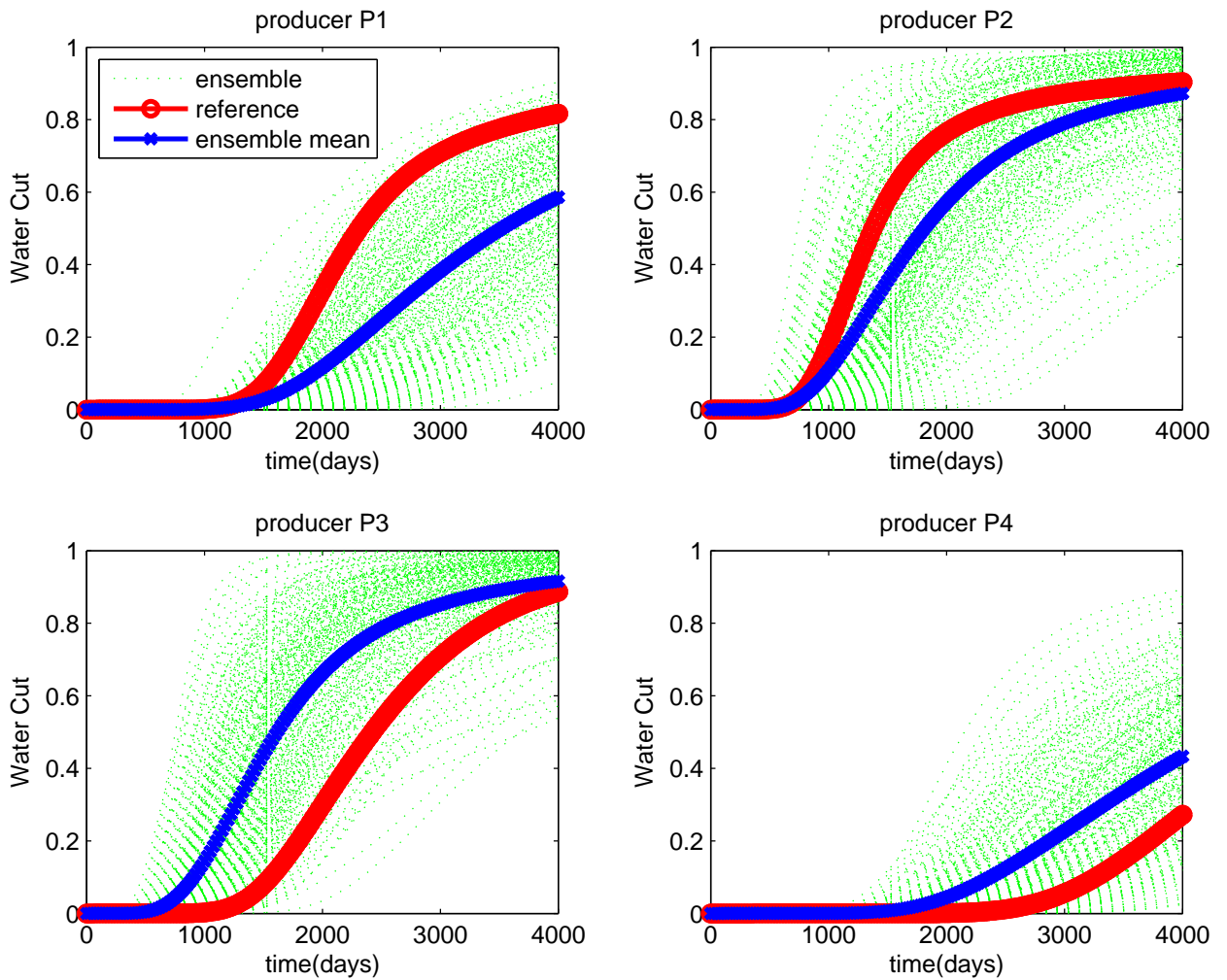


Fig. 4. Fractional flow prediction with 256 initial ensemble members (no data assimilation); ensemble members (green dots), ensemble mean (blue crosses) compared with true water cut data (red open circles); clockwise, production wells: 1 – 4.

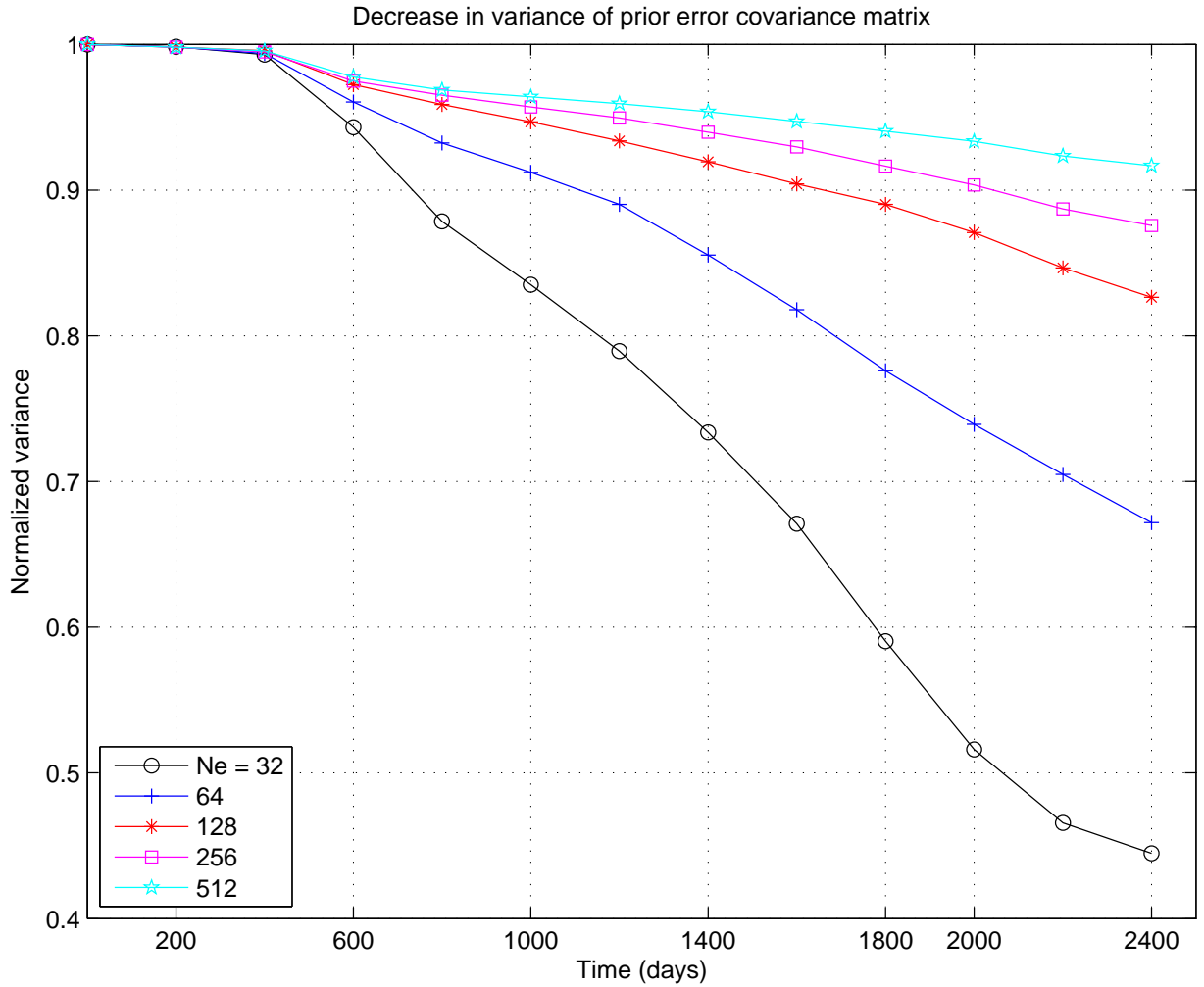


Fig. 5. Variance of error covariance  $\mathbf{P}^f$ , for all observation times, normalized by its initial value at time zero, for various ensemble sizes. Note that small ensemble sizes lead to insufficiently small variance. As we assimilate data, the all ensemble members *converge* to the truth, hence there will be a decrease in variance, as seen for larger  $N_e$  as well.

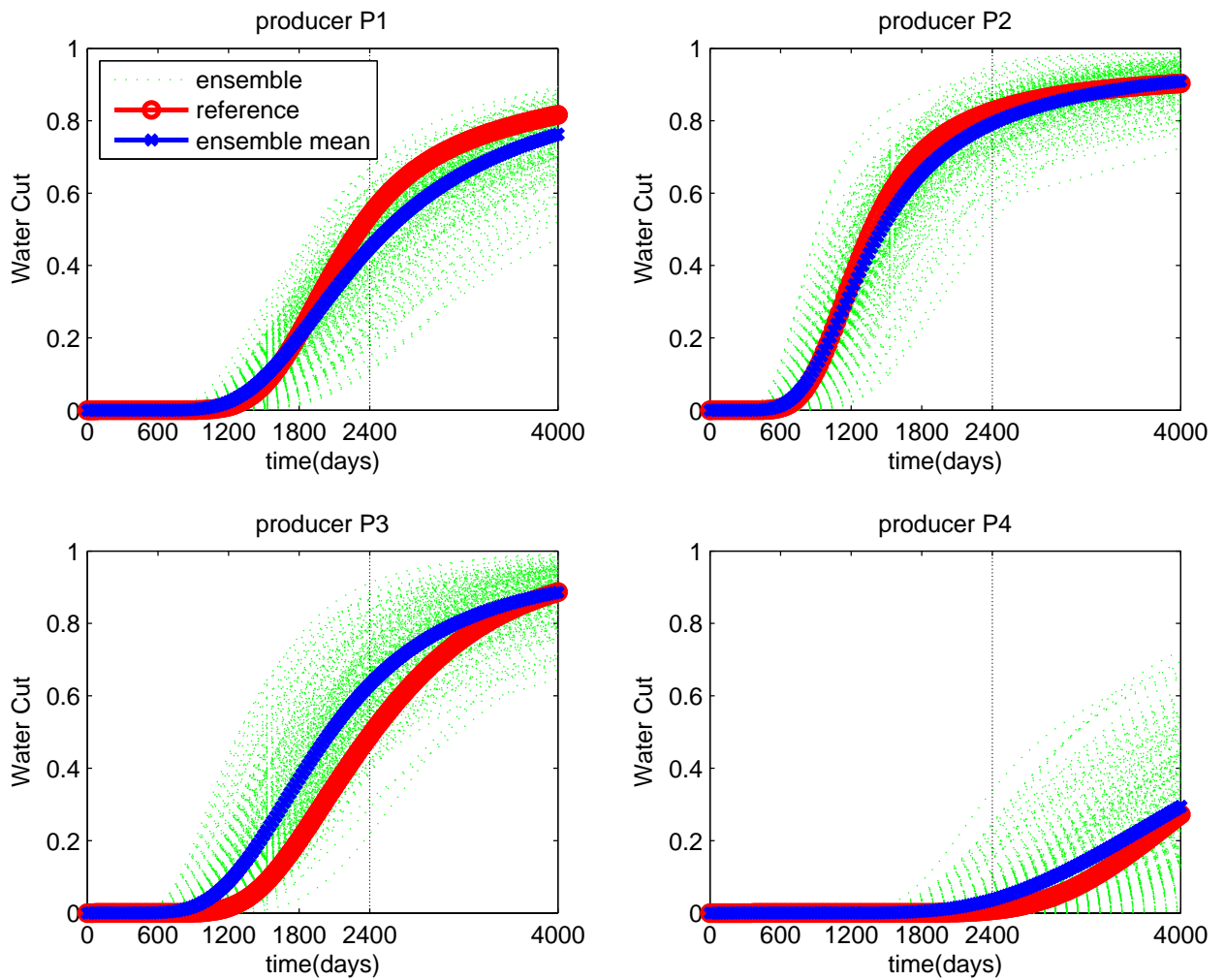


Fig. 6. Water cut prediction using assimilated (regular EnKF for 2400 days) ensemble members, note the improved fit of ensemble when compared to that in Fig. 4.

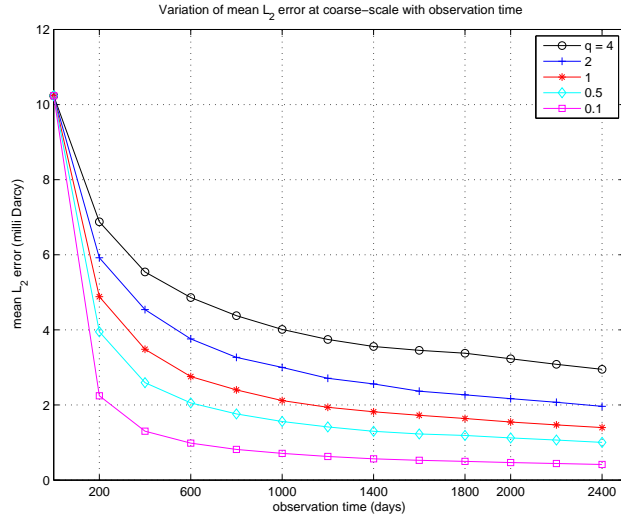
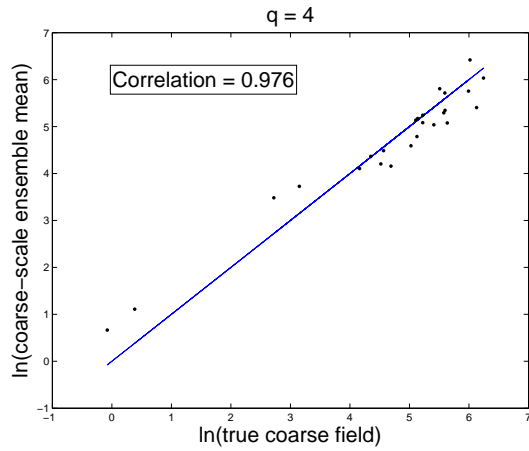
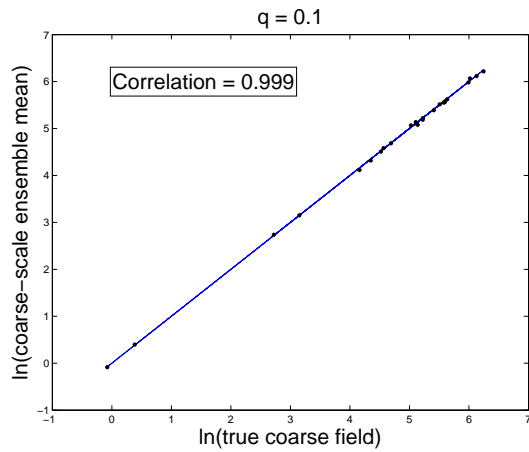


Fig. 7. Decrease in  $\bar{\epsilon}$  computed at coarse-scale, as data (fractional flow and  $5 \times 5$  coarse-scale permeability data at variance,  $\mathbf{Q} = q\mathbf{I}$ ) is assimilated using the coarse-scale EnKF algorithm.



(a)



(b)

Fig. 8. Correlation between coarse-scale ensemble mean and true permeability after assimilation for low and high precision in coarse data; (a) and (b):  $q = 4, 0.1$ .

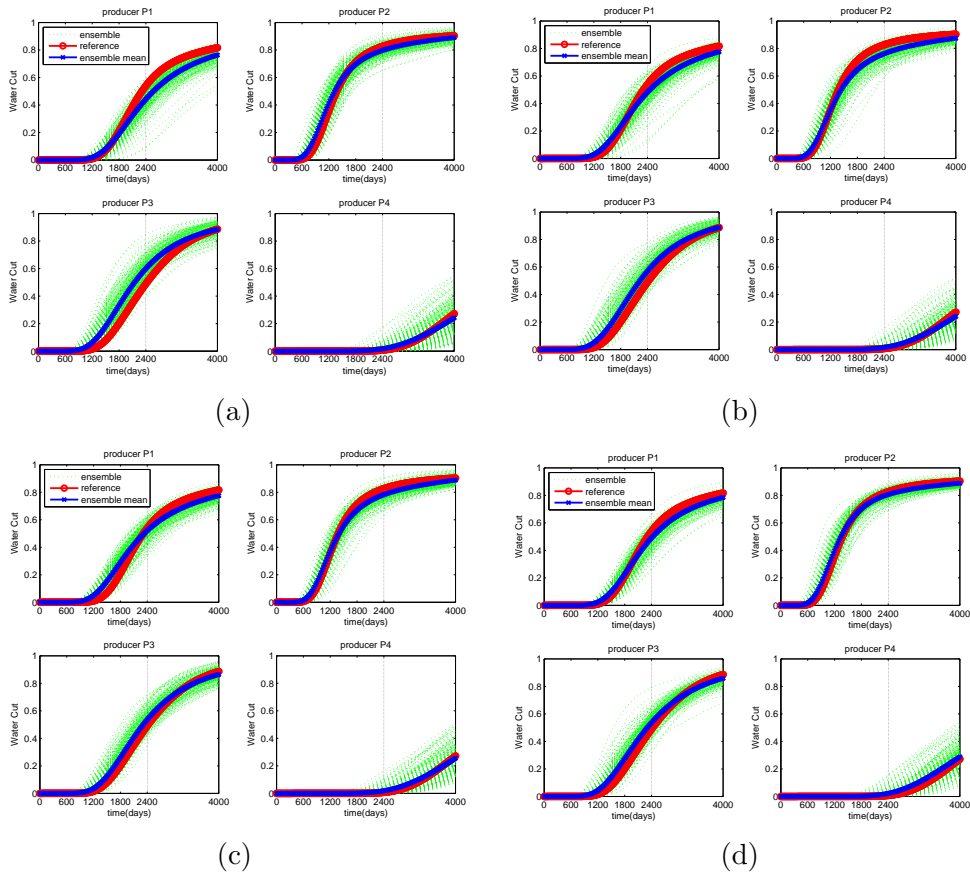


Fig. 9. Same as in Fig. 6, but using coarse-scale EnKF for data assimilation; clockwise, (a)– (d):  $q = 4, 2, 1, 0.1$ .

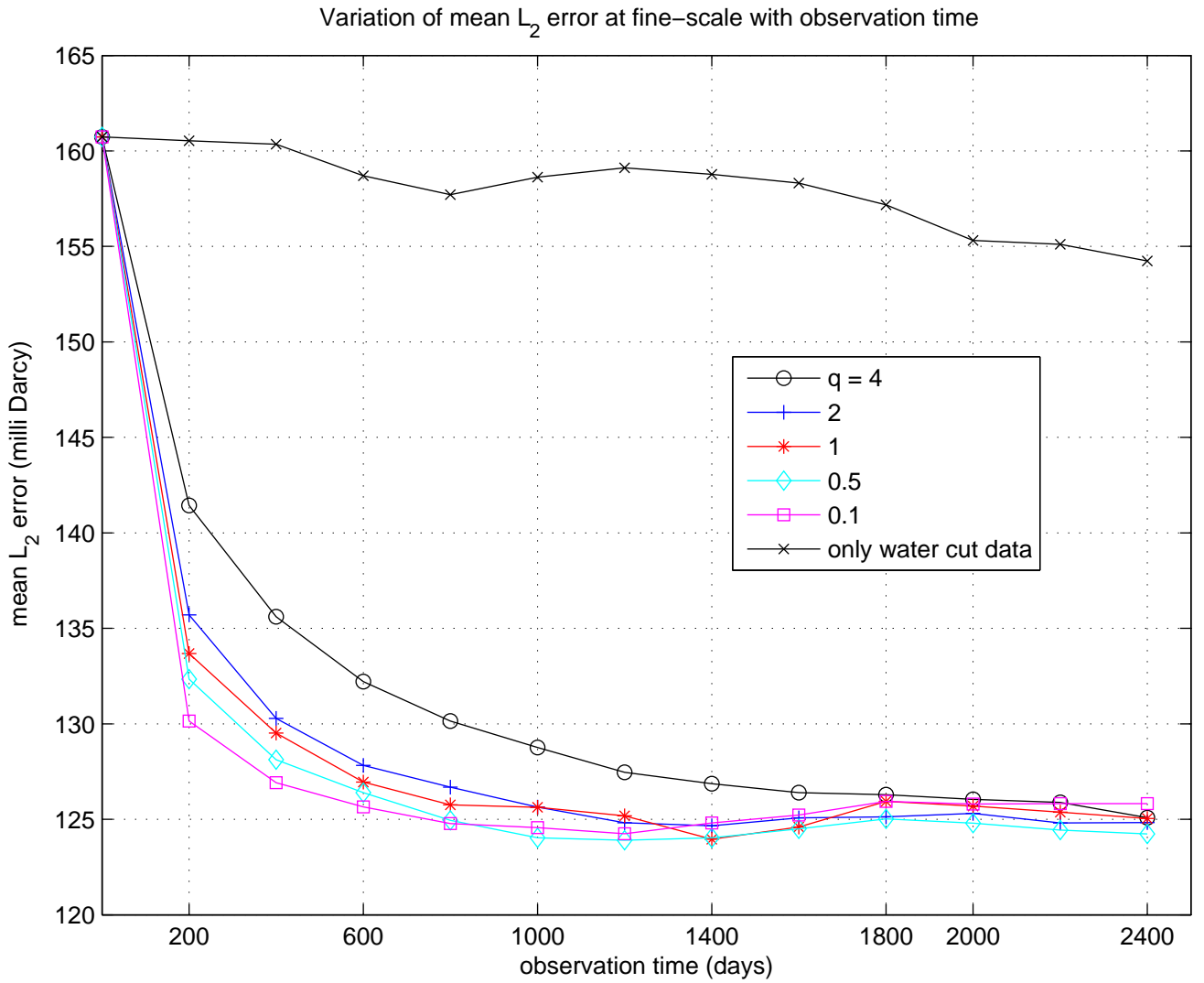


Fig. 10. Same as in Fig. 7, but at fine-scale, also shown is the error obtained with assimilation of fractional flow data only.

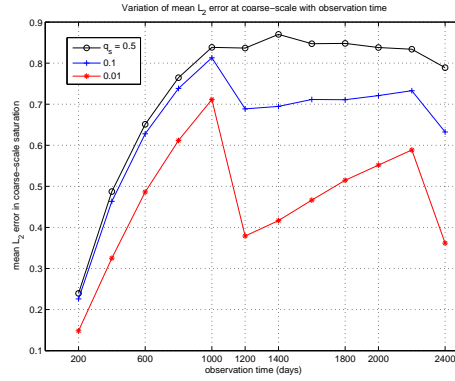


Fig. 11. Decrease in  $\bar{\epsilon}$  computed at coarse-scale, as data (fractional flow and  $5 \times 5$  coarse-scale saturation data at variance,  $\mathbf{Q} = q_s \mathbf{I}$ , supplied at 200, 1200 and 2400 days) is assimilated using the coarse-scale EnKF algorithm.

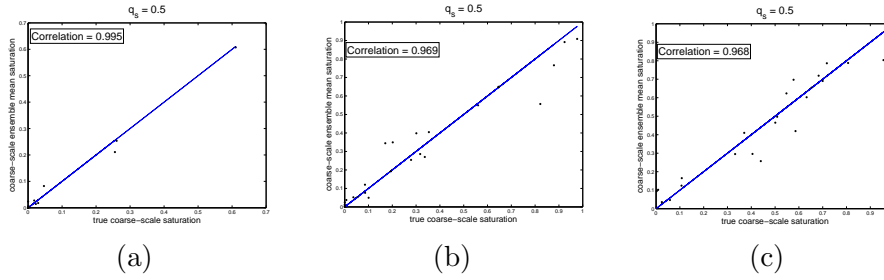


Fig. 12. Correlation between coarse-scale ensemble mean and true saturations after assimilation at time: left– right, 200, 1200 and, 2400 days.  $q_s = 0.5$ .

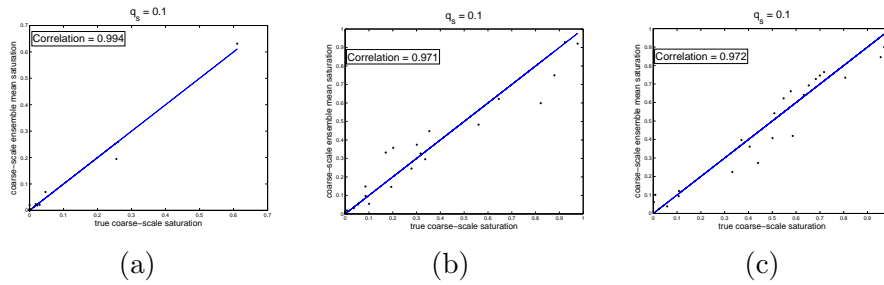


Fig. 13. Same as above, but with  $q_s = 0.1$ .

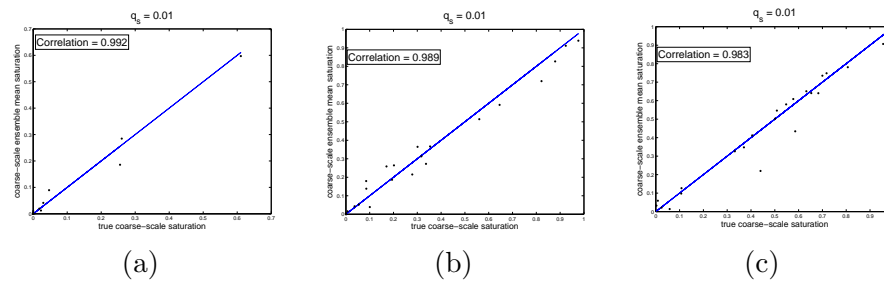
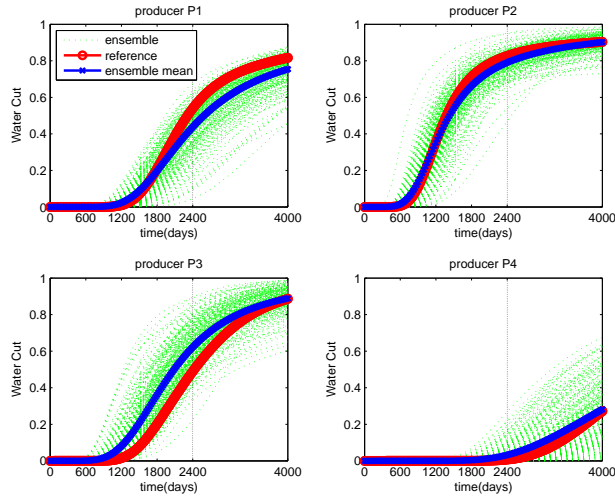
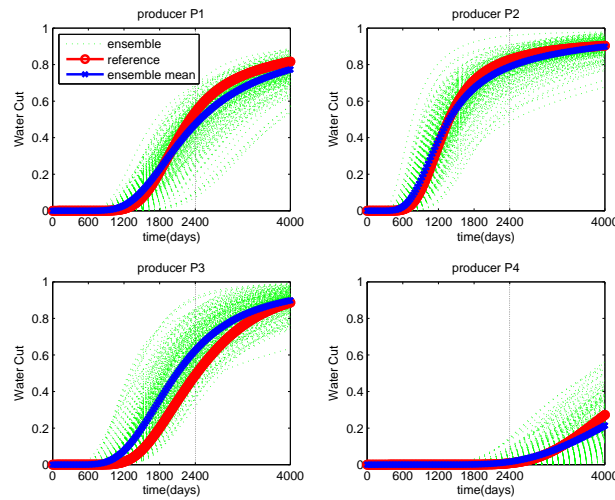


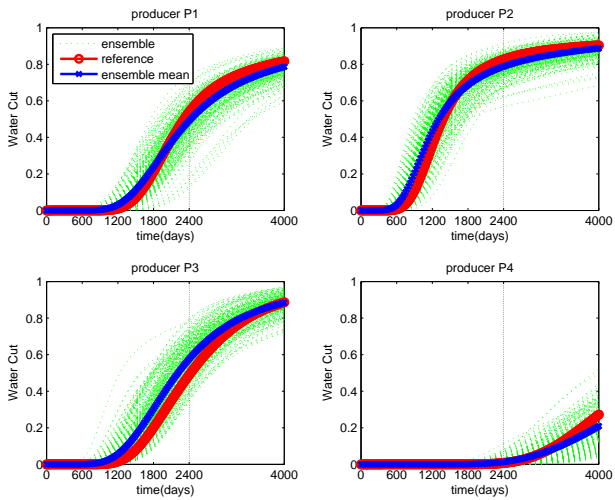
Fig. 14.  $q_s = 0.01$ .



(a)



(b)



(c)

Fig. 15. Same as in Fig. 9(d), but using coarse-scale EnKF for data assimilation of fractional flow and coarse-scale saturation; (a)– (c):  $q_s = 0.5, 0.1, 0.01$ . Note the improved fit of the ensemble (as in Fig. 15(c)) when compared to assimilation with regular EnKF Fig. 6.

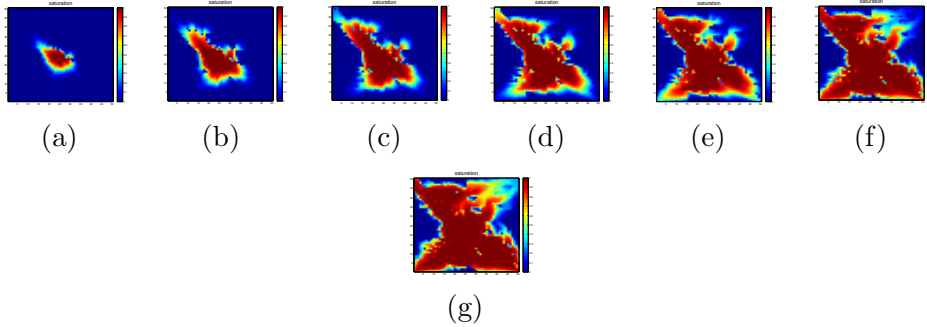


Fig. 16. Evolution true fine-scale saturation after (a) 200 days, (b) 600, (c) 1000, (d) 1500, (e) 2000, (f) 3000, (g) 4000, days. The initial saturation was specified to be zero.

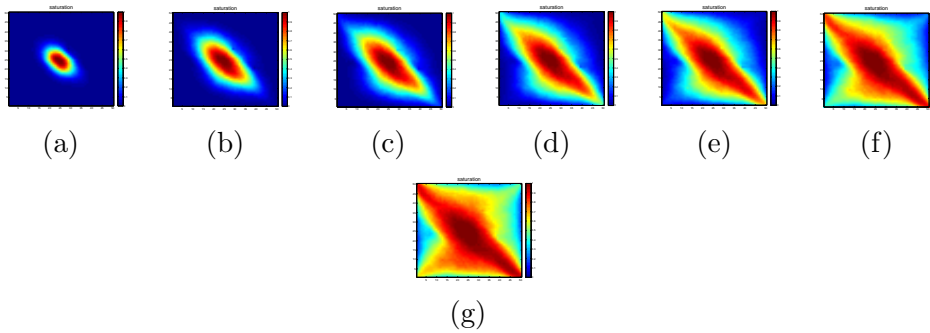


Fig. 17. Same as above, but prediction using the initial ensemble members (no data assimilation). We plot the ensemble mean saturation.

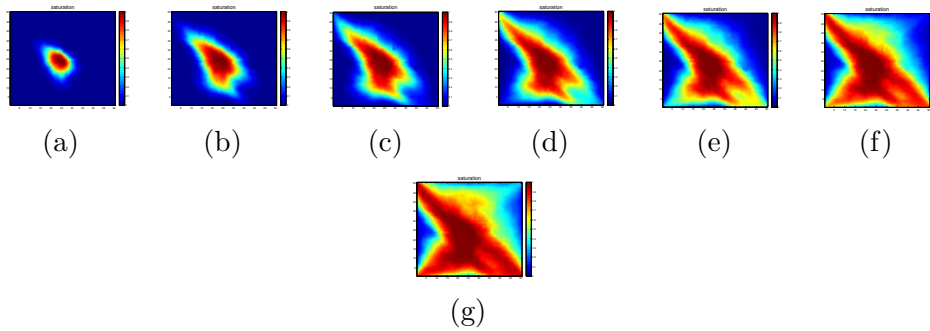


Fig. 18. Predicted ensemble mean using assimilated (regular EnKF with fractional flow data) ensemble members.

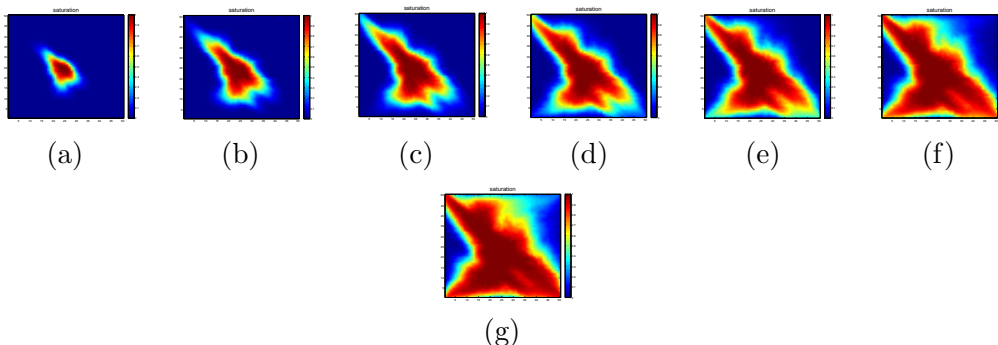


Fig. 19. Same as above, but assimilation was performed using coarse-scale EnKF with fractional flow and  $5 \times 5$  coarse-scale saturation data with variance,  $\mathbf{Q} = q_s \mathbf{I}$ ;  $q_s = 0.01$ . Observe that the ensemble mean saturation profile and history is more closer to the truth.

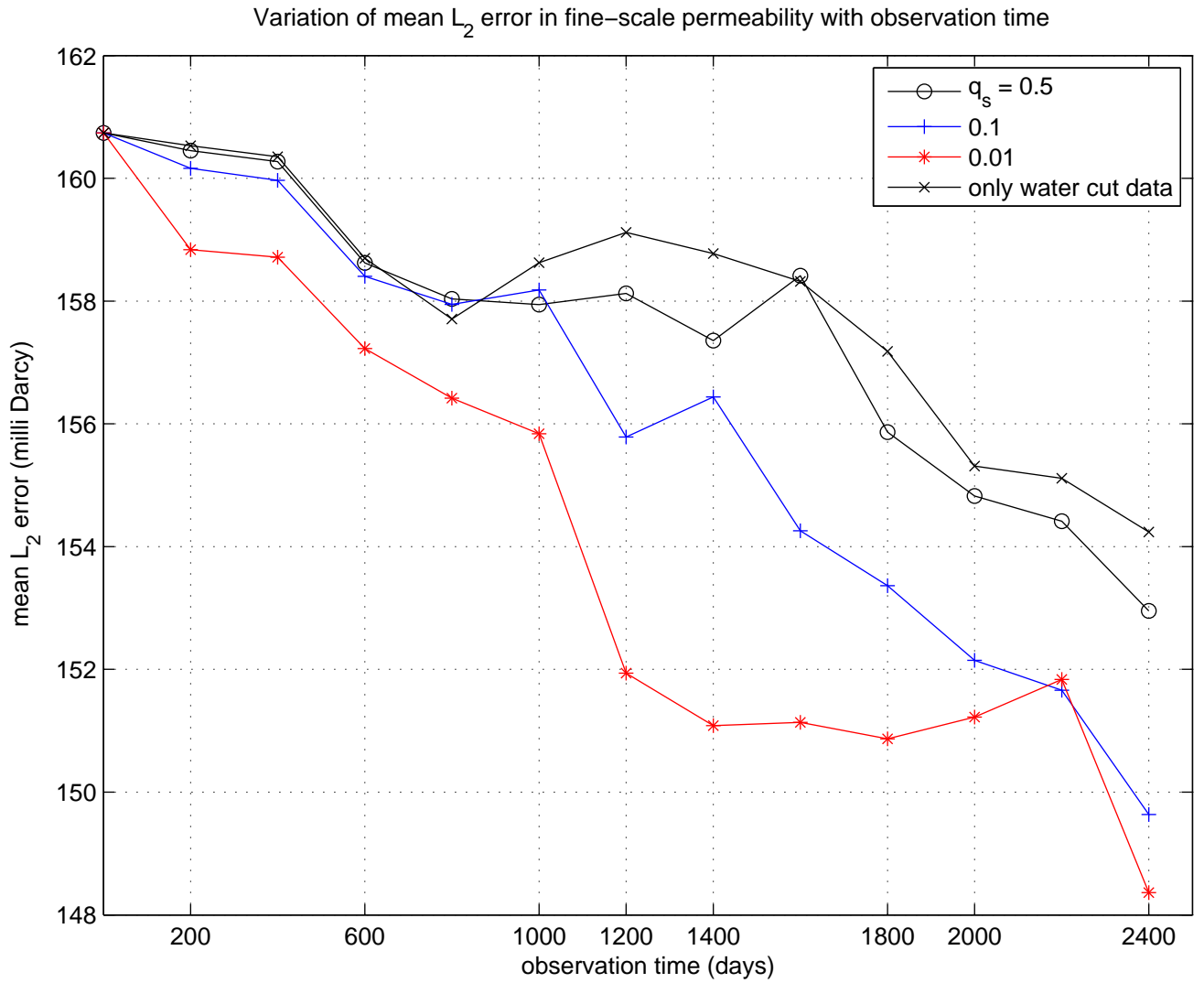


Fig. 20. Same as in Fig. 10, but with coarse-scale EnKF using observed fractional flow and coarse-scale saturation; the coarse-scale EnKF yields lesser error when compared to regular EnKF.

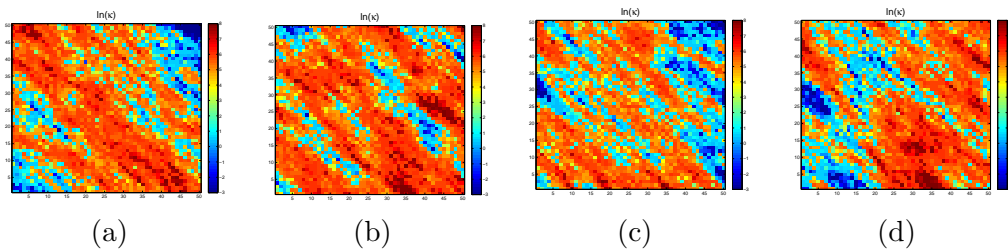


Fig. 21. Log permeabilities of a few  $i$ -th. initial ensemble members (before data assimilation); left–right, (a)  $i = 50$ , (b) 100, (c) 150, (d) 200.

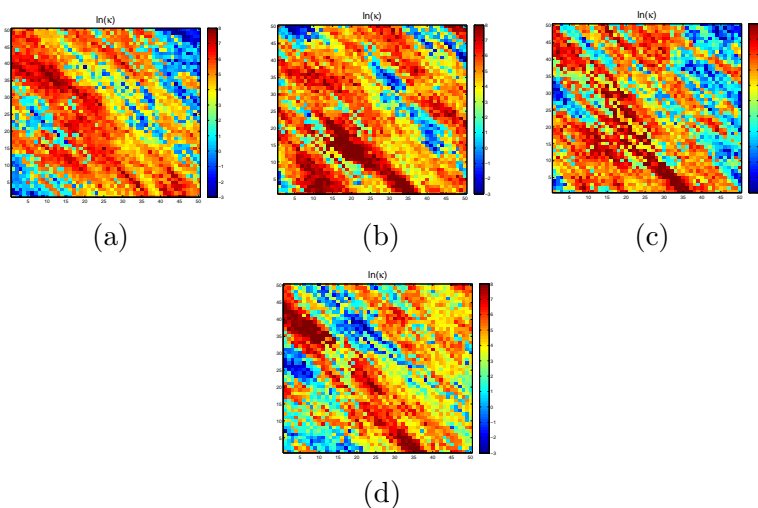


Fig. 22. Same as above, but after assimilating water cut data with regular EnKF.

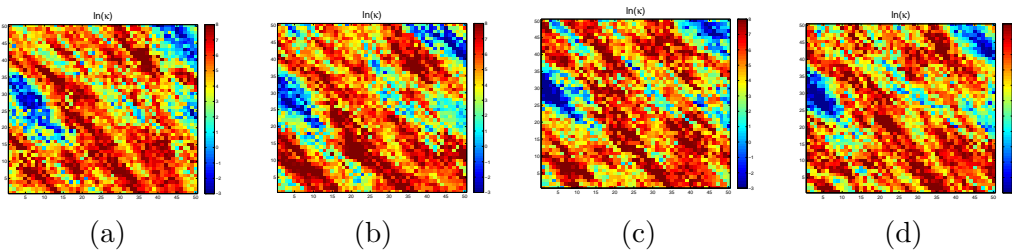


Fig. 23. Same as above, but assimilated using coarse-scale EnKF with  $q = 1$  for the variance of coarse-scale permeability data.

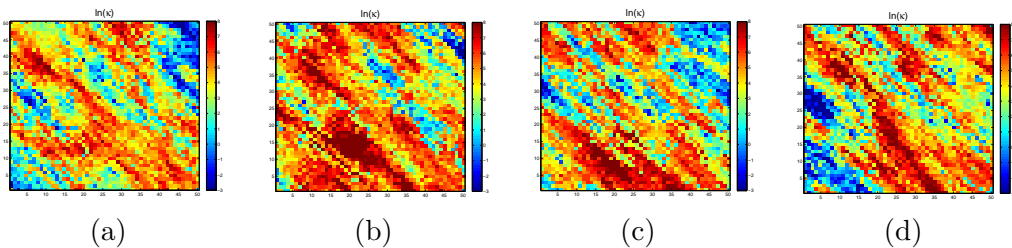


Fig. 24. As above, but assimilated using coarse-scale EnKF with coarse-scale saturation data, variance  $q_s = 0.01$ .

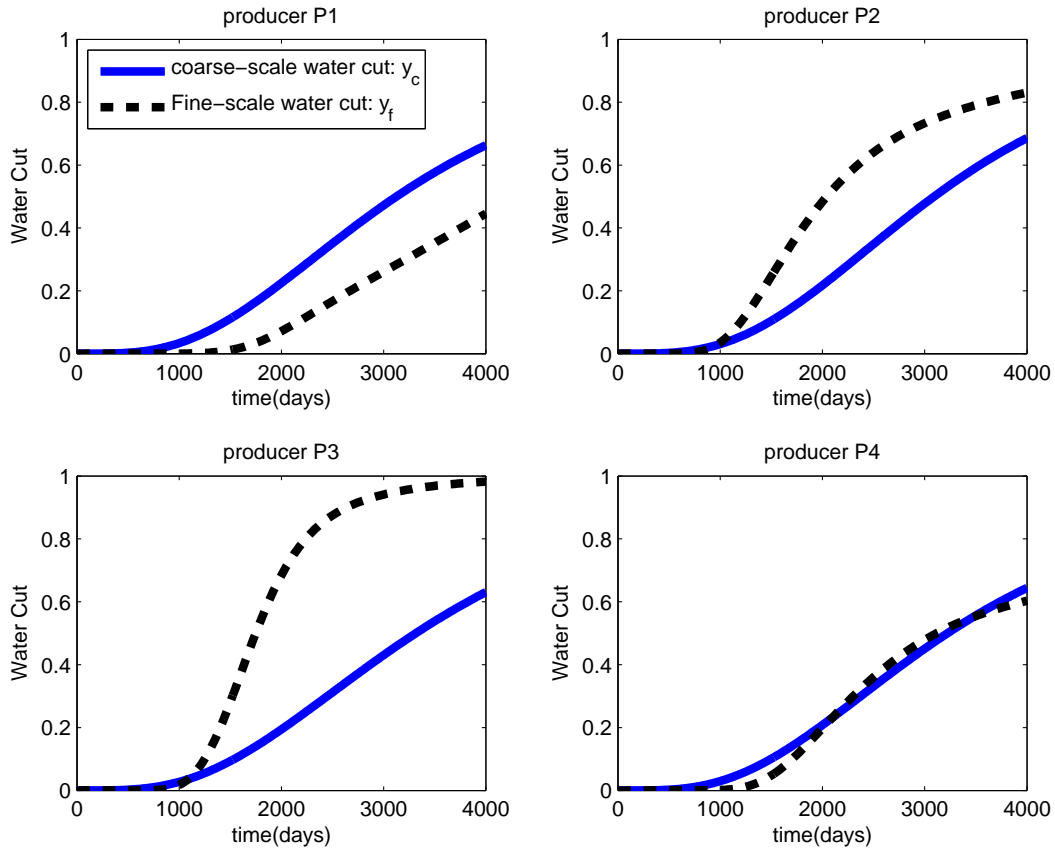


Fig. 25. Fine and coarse-scale water cut for an arbitrary ensemble member. The fine-scale permeability was upscaled using flow based upscaling to get the coarse-scale field. Fine-grid was 10 times coarsened in each direction to get the coarse-grid.

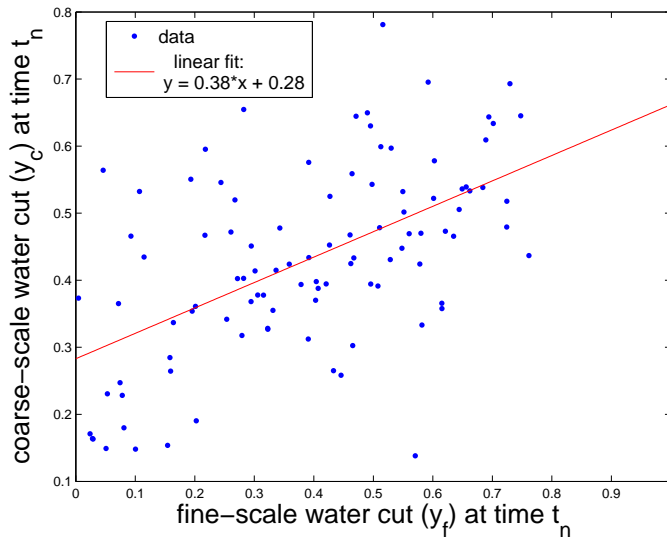


Fig. 26. Fine-scale ( $y_f$ ) versus coarse-scale ( $y_c$ ) water cut (producer P1,  $t_n = 3000$  days), for a sample size of 100; also shown is a linear fit between  $y_f$  and  $y_c$ .

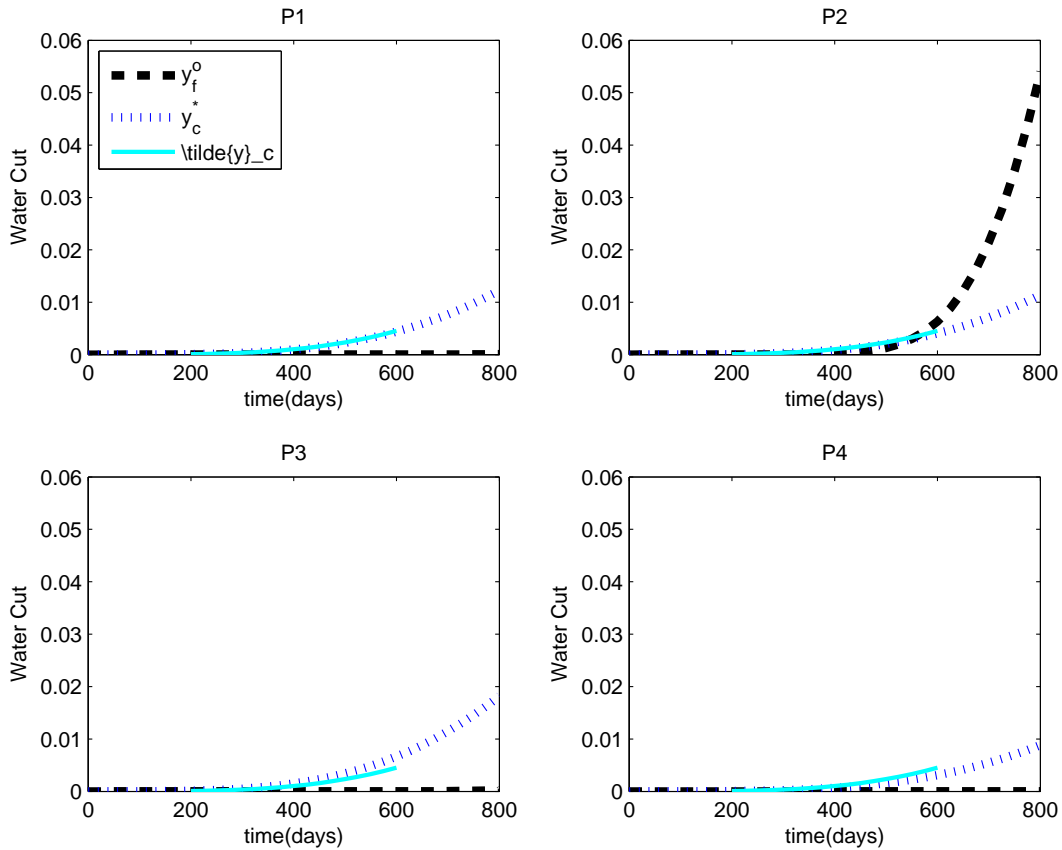


Fig. 27. A comparison of the fine-scale data ( $y_f^o$ ) mapped to the coarse-scale ( $\tilde{y}_c$ ) with the true coarse-scale water cut ( $y_c^*$ ). The linear least-squares mapping is described in section 5.1,  $y_f^o$  was mapped every 50 days, upto 600 days.

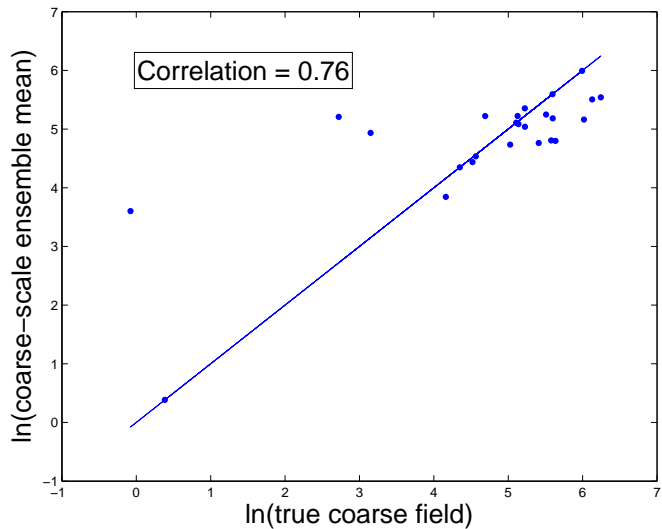


Fig. 28. Correlation between coarse-grid ensemble mean and reference coarse-scale permeabilities after data assimilation using EnKF on coarse-grid.  $\tilde{y}_c$  was used as observed data with standard deviation of 0.01